Summer 2019

Analyzing the effects of attitude errors when quantifying the on-orbit performance of a CubeSat micropropulsion system

Andrew Orion Watson

Department:

ANALYZING THE EFFECTS OF ATTITUDE ERRORS WHEN QUANTIFYING THE ON-ORBIT PERFORMANCE OF A CUBESAT MICROPROPULSION SYSTEM

by

ANDREW ORION WATSON

A THESIS

Presented to the Graduate Faculty of the

MISSOURI UNIVERSITY OF SCIENCE AND TECHNOLOGY

In Partial Fulfillment of the Requirements for the Degree

MASTER OF SCIENCE

in

AEROSPACE ENGINEERING

2019

Approved by

Dr. Henry Pernicka Advisor
Dr. Kyle DeMars
Dr. Serhat Hosder

ABSTRACT

CubeSats and small satellites have become popular methods of performing space research. Accordingly, interest has also grown in designing micropropulsion systems to increase the lifespan of these satellites. This work describes the framework for analyzing the effects of imperfect attitude determination and control when quantifying the on-orbit performance of a micropropulsion system. The Gauss variation of parameters equations were implemented to model the orbital mechanics, with perturbing models for the zonal harmonics, atmospheric drag, and solar radiation pressure included. Two common sources for imperfections in a spacecraft's attitude were considered. The first was to consider the effect of the spacecraft having poor pointing, done by varying the direction of the thrust due to attitude control errors. The second was to consider the effects of the accuracy of the attitude determination method, by incorporating sensor noise to the magnetometer and the Sun sensors used in the Quaternion Estimator (QUEST) algorithm.

ACKNOWLEDGMENTS

I am very grateful to my advisor, Dr. Hank Pernicka. For always assisting when I was struggling with a technical problem and for helping guide me in being able to complete my master's research. I will always value how you helped me improve both my technical and professional skills.

I would like to thank my committee members Dr. Kyle DeMars and Dr. Serhat Hosder for answering any questions I had along the way. I would also like to thank my friends and to everyone that I shared an office, it was a pleasure to be able to work with all of you. I would especially like to thank James Brouk and Donna Jennings. You both helped me think through challenging problems and provided insights that I would not have thought of on my own.

Lastly, I would like to thank my parents for all the hard work they have done to enable me to reach this far. It is because of all their love and support I was able to pursue my dreams.

TABLE OF CONTENTS

Page

APPENDICES

LIST OF ILLUSTRATIONS

Figure Page

LIST OF TABLES

Table Page

1. INTRODUCTION

Small satellites and CubeSats have created the opportunity for the design of simpler mission concepts that would be impractical to implement on large satellites. As technology improves CubeSat mission design is becoming more complex, including the options of formation flights and swarms of small satellites. To perform these missions requires these satellites to have precise attitude knowledge and a means of performing maneuvers to create the desired formation. Arcsecond level attitude accuracy can be achieved through the use of star trackers [1], however star trackers are generally costly, making them difficult to purchase for budget-limited CubeSat programs. Another means to determine the attitude of a satellite is to use two or more sensor measurements and solve Wahba's problem. This method typically provides attitude accuracy to within a degree [2].

The fidelity of an attitude solution is also dependent on the degree of perturbations that are considered in the model. While on orbit there are many perturbing forces that produce torques that affect a spacecraft's attitude, such as the gravity gradient, the magnetic dipole, atmospheric drag, and solar radiation pressure. While the torques produced by these perturbations is inherently small, they are often important to consider. Developing high fidelity models for these perturbations can be difficult due to the nonlinear nature of the perturbations and that they are often dependent on the physical properties of the spacecraft.

With the growing interest in performing formation flight missions, new propulsion systems are being designed specifically for CubeSats [3]. These new propulsion systems must be capable of performing maneuvers to place the CubeSats into the desired formation as well as performing smaller station-keeping maneuvers to maintain the formation. Electric propulsion systems can meet both of these requirements. However, quantifying an electric propulsion system's performance is difficult with ground-based testing because a vacuum environment is needed for the thruster to operate efficiently [4], as well as being unable to

reproduce the micro-gravity environment that would be experienced on-orbit. Therefore, to quantify the thrust produced by an electric propulsion system requires that it be operated on-orbit to accurately characterize its capabilities. This thesis study considers the effects of attitude pointing error on determining thrust from on-orbit GPS and IMU telemetry.

1.1. LITERATURE REVIEW

Extensive research has been done to characterize the thrust of spacecraft micro-propulsion systems by performing ground-based testing [5]-[8]. These types of ground-based tests are typically performed using either test stands, pendulum balances, or torsional balances in vacuum environments to simulate on-orbit performance. However, only a limited number of studies were found in the available literature verifying that the ground-based testing results and the performance of the thruster on-orbit show consistent thrust estimates.

The most direct method of determining the thrust of a maneuvering spacecraft is to measure the thrust with an accelerometer [9]. However, most low-cost accelerometers are not adequately accurate to measure the low thrust of an electric propulsion system, and the ones that can are very expensive. Another method of thrust determination is to perform orbit determination before and after the maneuver. By computing the change in the orbit, the required change in velocity (ΔV) can be determined, and by extension the thrust [10]. Both of these methods of thrust determination were compared against each other in the SERT II mission [11], where it was found that the thrust could be measured within 1% by the accelerometer and within 5% for the orbit changing maneuver.

A third method of thrust determination can be done by performing an attitude changing maneuver. By offsetting the thruster from the center of mass of the spacecraft a slewing maneuver can be performed to increase the angular velocity of the spacecraft, which can be measured directly with a gyroscope. With the change in angular velocity ($\Delta\omega$) and the length of the maneuver known, the thrust can be determined. This method was used by

[12] to determine the total ΔV produced by a micropropulsion system and [13] proposed a modification of the method to reduce noise effects, improving the thrust estimates to within 6% for simulations using $1\mu N$ thrust.

1.2. ADVANCED PROPULSION EXPERIMENT (APEX)

CubeSats follow a standard form factor where one unit is $10 \times 10 \times 10$ cm^3. When designing a CubeSat the most common limitations are size, weight, and power (SWaP). Because of these limitations many components that would typically be found on a conventional satellite are difficult to include; an example of this is propulsion systems that often require a large portion of the total mass and volume when integrated into a CubeSat. To overcome this limitation the Missouri University of Science and Technology's Satellite Research team is developing the Advanced Propulsion Experiment (APEX), a 6U CubeSat that hosts a new multi-mode micropropulsion system [14]. APEX is being designed as part of the University Nanosatellite Program (UNP)'s tenth cycle (NS-10). The current prototype version of APEX is shown in Figure 1.1. In this work APEX is described using the body-fixed frame shown in the bottom-left corner. The circle located in the middle of the panel that is aligned with the $b_2 - b_3$ plane represents the thruster of the micropropulsion system. For the majority of this work the thruster is assumed to be stationed at this location so that the thrust is applied through the geometric centroid of APEX.

The multi-mode micropropulsion system is capable of switching between high-thrust/low specific impulse (chemical) and low-thrust/high specific impulse (electric) modes [15]. The system uses the same propellant, feed system, and emitters for both modes of operation. The total mass and volume of this new system is approximately the same as either a chemical or electric propulsion system, while incorporating the thrusting capabilities of both.

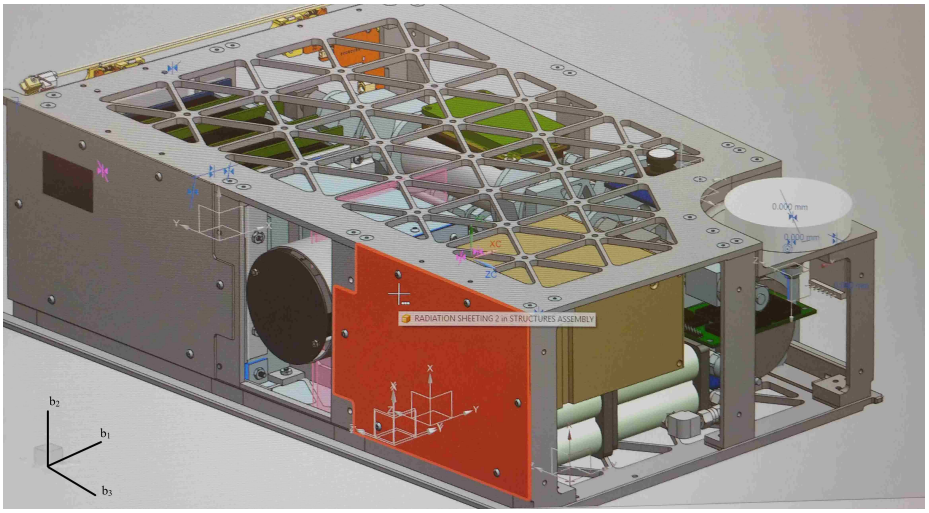

Figure 1.1. Prototype Design of APEX

Due to APEX's capability to execute both high and low thrust maneuvers it was chosen as a case study for this research. The primary goal of this research is to determine the effect attitude has on quantifying the performance of the multi-mode propulsion system in both chemical and electric modes.

1.3. THESIS ORGANIZATION

Section 2 discusses two-body and J_2 system dynamics, and shows a derivation of the Gauss variation of parameters for both systems. The attitude dynamics, and the perturbation models for atmospheric drag and solar radiation pressure are given as well. Section 3 shows a derivation of an analytic method for thrust determination when performing an orbit changing maneuver and an attitude changing maneuver. Section 4 shows the derivations for Davenport's q-method and the quaternion estimator (QUEST) method of attitude determination. Section 5 describes the simulations created to perform an orbit changing and an attitude changing maneuver for the case study APEX. Section 6 discusses the findings of the simulations and the benefits of choosing both maneuver types for thrust determination.

2. SYSTEM DYNAMICS

2.1. TWO-BODY DYNAMICS

The Gauss variation of parameter (VOP) equations define the rate of change of the Keplerian orbital elements when acted upon by a perturbing force. Because the VOP equations are evaluated in terms of the Local Vertical Local Horizontal (LVLH) frame, perturbations acting on the spacecraft can be relatively easily accounted for as the summation of the perturbing forces. The LVLH frame axes are defined as $\hat{r}$, $\hat{\theta}$, and $\hat{h}$, as shown in Figure 2.1, where $\hat{r}$ is along the radial direction, $\hat{h}$ is normal to the orbit plane, and $\hat{\theta}$ completes the right-handed triad (for circular orbits $\hat{\theta}$ coincides with the velocity direction). From Battin [16] the Gauss VOP equations can be written as a function of the perturbing accelerations f_r, f_θ, and f_h as

$$\frac{da}{dt} = \frac{2a^2}{h}\left(e\sin(\nu)f_r + \frac{p}{r}f_\theta\right) \tag{2.1}$$

$$\frac{de}{dt} = \frac{1}{h}\left[p\sin(\nu)f_r + \big((p+r)\cos(\nu) + re\big)f_\theta\right] \tag{2.2}$$

$$\frac{di}{dt} = \frac{r\cos\theta}{h}f_h \tag{2.3}$$

$$\frac{d\Omega}{dt} = \frac{r\sin\theta}{h\sin i}f_h \tag{2.4}$$

$$\frac{d\omega}{dt} = \frac{1}{eh}\left[-p\cos(\nu)f_r + (p+r)\sin(\nu)f_\theta\right] - \frac{r\sin\theta\cos i}{h\sin i}f_h \tag{2.5}$$

$$\frac{d\nu}{dt} = \frac{h}{r^2} + \frac{1}{eh}\left[p\cos(\nu)f_r - (p+r)\sin(\nu)f_\theta\right] \tag{2.6}$$

where r is the orbital radius, p is the semi-parameter, h is the specific angular momentum, and θ is the argument of latitude, given by

$$r = \frac{a(1-e^2)}{1+e\cos\nu} \qquad p = a(1-e^2) \qquad h = \sqrt{\mu a(1-e^2)} \qquad \theta = \omega + \nu$$

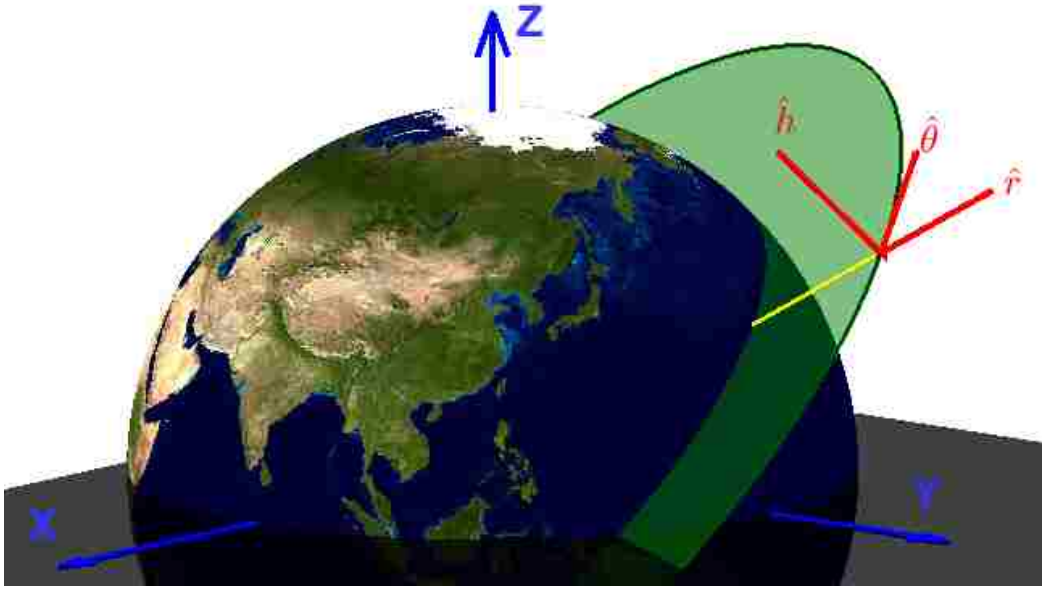

Figure 2.1. Local Vertical Local Horizontal (LVLH) Frame

The Earth Centered Inertial (ECI) frame is a commonly used inertial frame in orbital analyses. Specifically, this work uses the J2000 epoch to fix the axes for which the x-axis aligns with the vernal equinox, the z-axis aligns with the North Pole, and the y-axis completes the right-handed triad. The J2000 epoch is defined from the Julian Date for January 1, 2000, at noon Terrestrial Time. As seen in Vallado [17] the Julian date for the J2000 epoch is exactly 2451545.0 Terrestrial Time and can be determined from

$$\begin{aligned} JD(Y,M,D,h,m,s) =& 1,721,013.5 + 367Y - \text{INT}\left\{\frac{7}{4}\left[Y + \text{INT}\left(\frac{M+9}{12}\right)\right]\right\} \\ &+ \text{INT}\left(\frac{275M}{9}\right) + D + \frac{60h + m + s/60^*}{1440} \end{aligned} \tag{2.7}$$

where INT denotes "flooring" (truncating) the value to the nearest integer and 60^* denotes using 61 seconds for days with a leap second. An example of how to calculate the Julian date for April 30, 2019, at noon Terrestrial Time is provided:

$$
\begin{aligned}
JD(2019,4,30,12,0,0) =& 1,721,013.5 + (367 * 2019 - \text{INT}\left\{\frac{7}{4}\left[2019 + \text{INT}\left(\frac{4+9}{12}\right)\right]\right\} \\
&+ \text{INT}\left(\frac{275*4}{9}\right) + 30 + \frac{60*12+0+0/60^*}{1440} \\
=& 1,721,013.5 + 740973 - \text{INT}\left\{\frac{7}{4}\left[2019 + \text{INT}\left(1.0833\right)\right]\right\} \\
&+ \text{INT}\left(122.222\right) + 30 + 0.5 \\
=& 2462017.0 - \text{INT}\left\{\frac{7}{4}\left[2019 + \text{INT}\left(1.0833\right)\right]\right\} + \text{INT}\left(122.222\right) \\
=& 2462017.0 - \text{INT}\left\{\frac{7}{4}\left[2019 + 1\right]\right\} + 122 \\
=& 2462139.0 - \text{INT}\left\{3535\right\} \\
=& 2458604.0
\end{aligned}
$$

When using multiple coordinate frames it is convenient to define direction cosine rotation matrices between them. To transform coordinates from the ECI to the LVLH frame the following equations can be used:

$$
\hat{r} = \frac{\vec{r}}{||\vec{r}||} \qquad \hat{h} = \frac{\vec{r} \times \vec{v}}{||\vec{r} \times \vec{v}||} \qquad \hat{\theta} = \hat{h} \times \hat{r}
$$

where $\vec{r}$ is the position vector and $\vec{v}$ is the velocity vector of the spacecraft with respect to the ECI frame. From these equations a rotation matrix can be defined as

$$
C_{ECI}^{LVLH} = \begin{bmatrix} \hat{r}^T \\ \hdashline \hat{\theta}^T \\ \hdashline \hat{h}^T \end{bmatrix} \tag{2.8}
$$

To transform coordinates from the LVLH to the ECI frame is simply the transpose of the previous matrix

$$
C_{LVLH}^{ECI} = (C_{ECI}^{LVLH})^T = \left[\begin{array}{c:c:c} \hat{r} & \hat{\theta} & \hat{h} \end{array}\right] \tag{2.9}
$$

2.2. ATTITUDE DYNAMICS

The attitude of a spacecraft can be defined through many different vector or matrix representations. This author chose to use quaternions because they are a minimum-component attitude representation that avoids singularities. A quaternion $\mathbf{q}$ is the combination of a three-component vector $\mathbf{q}_{1:3}$ and a scalar q_4, given by

$$\mathbf{q} = \begin{bmatrix} \mathbf{q}_{1:3} \\ q_4 \end{bmatrix} \quad \text{where} \quad \mathbf{q}_{1:3} = \begin{bmatrix} q_1 \\ q_2 \\ q_3 \end{bmatrix} \tag{2.10}$$

Because quaternions are a four-component representation of a three-dimensional space, they are subject to a single constraint that they must maintain the unit norm

$$\|\mathbf{q}\|^2 = \|\mathbf{q_{1:3}}\|^2 + q_4^2 = 1 \tag{2.11}$$

An important property to consider when using quaternions is that they cannot be directly added together because they are an attitude representation. To be able to take the product of two quaternions requires a special operation defined as

$$\bar{\mathbf{q}} \otimes \mathbf{q} = \begin{bmatrix} q_4\bar{\mathbf{q}}_{1:3} + \bar{q}_4\mathbf{q}_{1:3} - \bar{\mathbf{q}}_{1:3} \times \mathbf{q}_{1:3} \\ \bar{q}_4 q_4 - \bar{\mathbf{q}}_{1:3} \cdot \mathbf{q}_{1:3} \end{bmatrix} \tag{2.12}$$

Quaternions can also be expressed as a 3×3 attitude matrix given by

$$A(\mathbf{q}) = \begin{bmatrix} q_1^2 - q_2^2 - q_3^2 + q_4^2 & 2\,(q_1q_2 + q_3q_4) & 2\,(q_1q_3 - q_2q_4) \\ 2\,(q_2q_1 - q_3q_4) & -q_1^2 + q_2^2 - q_3^2 + q_4^2 & 2\,(q_2q_3 + q_1q_4) \\ 2\,(q_3q_1 + q_2q_4) & 2\,(q_3q_2 - q_1q_4) & -q_1^2 - q_2^2 + q_3^2 + q_4^2 \end{bmatrix} \tag{2.13}$$

Just like an inverse attitude matrix can be defined, the inverse quaternion is defined as

$$\mathbf{q}^{-1} = \begin{bmatrix} -\mathbf{q}_{1:3} \\ q_4 \end{bmatrix}$$

Due to perturbations the attitude of a spacecraft is generally not inertially fixed, therefore it is useful to know how the quaternion changes with respect to time. The kinematic equation for a quaternion rate of change can be defined by representing the angular velocity vector $\boldsymbol{\omega}$ as a pure quaternion $\mathbf{w}$ i.e.

$$\dot{\mathbf{q}} = \frac{1}{2}\mathbf{w} \otimes \mathbf{q} \quad \text{where} \quad \mathbf{w} = \begin{bmatrix} \boldsymbol{\omega} \\ 0 \end{bmatrix} \tag{2.14}$$

In this work, the quaternion represents the rotation from the spacecraft body frame to the LVLH frame.

2.3. PERTURBATIONS

2.3.1. Zonal Harmonics. A significant source of perturbations in low Earth orbit are effects of nonspherical gravitational harmonics. The disturbing potential function for these nonspherical effects, R, is modeled as

$$\begin{aligned} R = -\frac{\mu}{r}\Bigg[\sum_{\ell=2}^{\infty} J_\ell \left(\frac{R_\oplus}{r}\right)^\ell P_{\ell,0}[\sin(\phi_{gc})] \\ + \sum_{\ell=2}^{\infty}\sum_{m=1}^{\ell} \left(\frac{R_\oplus}{r}\right)^\ell P_{\ell,m}[\sin(\phi_{gc})][C_{\ell,m}\cos(m\lambda) + S_{\ell,m}\sin(m\lambda)]\Bigg] \end{aligned} \tag{2.15}$$

where $R_\oplus$ is the radius of the Earth, J_ℓ are the zonal harmonic coefficients, $C_{\ell,m}$ and $S_{\ell,m}$ are the gravitational coefficients, ϕ_{gc} is the spacecraft geocentric latitude, λ is the spacecraft longitude, $P_{\ell,m}[\sin(\phi_{gc})]$ are the associated Legendre functions, and ℓ and m are the Legendre polynomial degree and order. For reference the zonal harmonics are defined for when $m = 0$ and examples for $\ell = 2$ through 5 can be seen in Figure 2.2 [17].

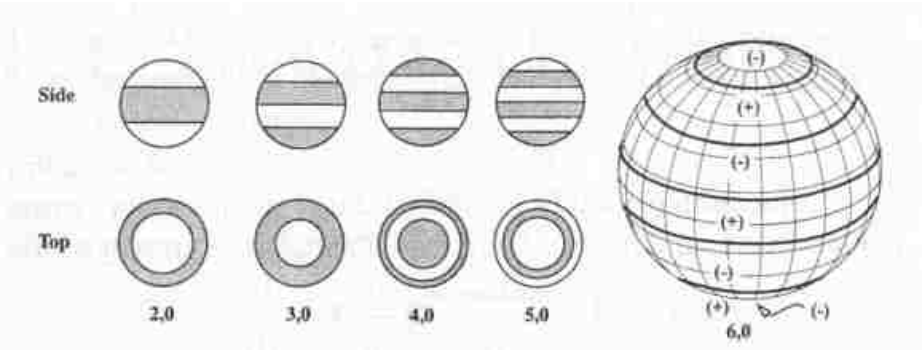

Figure 2.2. Zonal Harmonics for $\ell = 2$ through 5, $m = 0$ (taken from [17])

The disturbing potential function summations account for all of the nonspherical variations in the shape of the Earth, however it is often approximated by considering only the term for the oblateness of the Earth, J_2. This reduction to only use the J_2 term can be done by defining $\ell = 2$, $m = 0$ and neglecting the sectoral and tesseral harmonic terms, resulting in

$$R = -\frac{\mu J_2}{r}\left(\frac{R_\oplus}{r}\right)^2 P_{2,0}[\sin(\phi_{gc})] \tag{2.16}$$

This equation can be rewritten in Keplerian elements as

$$\begin{aligned} R &= -\frac{\mu J_2}{r}\left(\frac{R_\oplus}{r}\right)^2 P_{2,0}\left[\sin\left(\phi_{gc}\right)\right] && \text{where} \quad P_{2,0}[\sin(\phi_{gc})] = \frac{3}{2}\left(\sin^2(\phi_{gc}) - \frac{1}{3}\right) \\ &= -\frac{\mu J_2}{r}\left(\frac{R_\oplus}{r}\right)^2 \frac{3}{2}\left(\sin^2\left(\phi_{gc}\right) - \frac{1}{3}\right) && \text{where} \quad \sin\left(\phi_{gc}\right) = \sin i \sin\theta \\ &= -\frac{3\mu J_2 R_\oplus^2}{2r^3}\left(\sin^2 i \sin^2\theta - \frac{1}{3}\right) \end{aligned} \tag{2.17}$$

Now the disturbing potential function for J_2 can be directly applied to the Gauss VOP equations by taking the vector gradient of the function in spherical coordinates to acquire the acceleration components in terms of the LVLH frame as

$$\begin{aligned} f_{r,J_2} &= \frac{\partial R}{\partial r} = \frac{\partial}{\partial r}\left[-\frac{3\mu J_2 R_\oplus^2}{2r^3}\left(\sin^2 i \sin^2\theta - \frac{1}{3}\right)\right] \\ &= \frac{9\mu J_2 R_\oplus^2}{2r^4}\left(\sin^2 i \sin^2\theta - \frac{1}{3}\right) \end{aligned} \tag{2.18}$$

$$\begin{aligned} f_{\theta,J_2} &= \frac{1}{r}\frac{\partial R}{\partial \theta} = \frac{1}{r}\frac{\partial}{\partial \theta}\left[-\frac{3\mu J_2 R_\oplus^2}{2r^3}\left(\sin^2 i \sin^2\theta - \frac{1}{3}\right)\right] \\ &= -\frac{3\mu J_2 R_\oplus^2}{r^4}\left(\sin^2 i \cos\theta \sin\theta\right) \end{aligned} \tag{2.19}$$

$$\begin{aligned} f_{h,J_2} &= \frac{1}{r\sin\theta}\frac{\partial R}{\partial i} = \frac{1}{r\sin\theta}\frac{\partial}{\partial i}\left[-\frac{3\mu J_2 R_\oplus^2}{2r^3}\left(\sin^2 i \sin^2\theta - \frac{1}{3}\right)\right] \\ &= -\frac{3\mu J_2 R_\oplus^2}{r^4}\left(\cos i \sin i \sin\theta\right) \end{aligned} \tag{2.20}$$

2.3.2. Atmospheric Drag. For spacecraft in low Earth orbit atmospheric drag is often the largest source of external perturbing torque. To model the atmospheric drag the spacecraft is assumed to be composed of a series of flat plates with the force being applied to the center of pressure of each plate. For CubeSats this is often a reasonable representation of the actual spacecraft due to their simple geometry. For larger spacecraft this is not always the case because of the likelihood of having more complex geometry, for which a flat plate is an inaccurate representation. For the flat plate model the aerodynamic force experienced by a plate is modeled as

$$\mathbf{F}^i_{\text{drag}} = -\frac{1}{2}\rho c_D \left\|\mathbf{v}_{\text{rel}}\right\| \mathbf{v}_{\text{rel}B} S_i \cos\theta^i_{\text{drag}} \tag{2.21}$$

where ρ is the atmospheric density, c_D is the drag coefficient, $\mathbf{v}_{\text{rel}}$ is the relative velocity with respect to the Earth (because the atmosphere is assumed to rotate with the Earth), S is the area of the plate, and θ_{drag} is the angle of the relative velocity to the normal of each plate. It

is important to note that at any given time only the three leading faces of the spacecraft will experience a drag force. Therefore when $\cos\theta_{\text{drag}}$ is negative the drag force for that plate is set to zero. The drag coefficient was chosen as 2.2, as this is often approximately the value when using a flat plate model for spacecraft in upper atmosphere [17]. The atmospheric density ρ was modeled using a fully static, exponentially decaying model that can be found in [18]. This model has no time dependence and is purely a function of the current height above sea level. The relative velocity of the spacecraft in the body frame is

$$\mathbf{v}_{relB} = A^T C_{ECI}^{LVLH} \begin{bmatrix} \dot{x} + \omega_{\oplus} y \\ \dot{y} - \omega_{\oplus} x \\ \dot{z} \end{bmatrix} \tag{2.22}$$

where x, y, and z are ECI coordinates of the spacecraft, $\omega_{\oplus} = 0.000072921158553$ rad/s is the Earth's angular speed, and A^T is the rotation matrix from the LVLH to the body frame. The total force due to atmospheric drag can then be written as

$$\mathbf{F}_{\text{drag}} = \sum_{i=1}^{N} F^i_{r,\text{drag}}\hat{r} + F^i_{\theta,\text{drag}}\hat{\theta} + F^i_{h,\text{drag}}\hat{h} \tag{2.23}$$

From the total force the perturbing acceleration in terms of the LVLH frame is

$$\mathbf{f}_{\text{drag}} = A\frac{\mathbf{F}_{\text{drag}}}{m} \tag{2.24}$$

The total torque is the summation of the torques experienced by the individual plates given by

$$\mathbf{L}_{\text{drag}} = \sum_{i=1}^{N} \mathbf{r}^i \times \mathbf{F}^i_{\text{drag}} \tag{2.25}$$

where $\mathbf{r}^i$ the position vector from the center of mass of the spacecraft to the center of pressure of each plate.

2.3.3. Solar Radiation Pressure. Solar radiation pressure (SRP) is another perturbation source, though in low-Earth orbit it is much less of a concern compared to atmospheric drag. It is not until an altitude of approximately 800 km that SRP has more of an effect than atmospheric drag [18]. An important consideration is that when the spacecraft is shadowed by the Earth the SRP is zero. Similar to the atmospheric drag, to define the SRP, the spacecraft is modeled as a series of flat plates with the SRP force being applied to the center of pressure of the plate. From Vallado [17] the force applied to a plate is modeled as

$$\mathbf{F}_{\text{SRP}} = -P_{\odot} S_i \left[2 \left(\frac{R^i_{\text{diff}}}{3} + R^i_{\text{spec}} \cos\theta^i_{\text{SRP}} \right) \mathbf{n}^i_B + \left(1 - R^i_{\text{spec}} \right) \mathbf{s} \right] \max\left(\cos\theta^i_{\text{SRP}}, 0 \right) \tag{2.26}$$

where i denotes a specific plate in the series, and the variables are the solar radiation pressure $P_{\odot}$, the area of the plate S, the diffuse reflection coefficient R_{diff}, the specular reflection coefficient R_{spec}, the outward normal in the body coordinate frame $\mathbf{n}_B$, the spacecraft-to-Sun unit vector in the body frame $\mathbf{s}$, and the angle between the Sun vector and the normal to the plate $\cos\theta_{\text{SRP}}$. To determine the solar radiation pressure it is necessary to determine the position of the Sun relative to the spacecraft; the procedure to do so follows from [18]. The first step is to determine the mean longitude, $\phi_{\odot}$, and the mean anomaly of the Sun, $M_{\odot}$, in degrees as

$$\phi_{\odot} = 280.460^{\circ} + 36{,}000.771\ T_{UT1} \tag{2.27}$$

$$M_{\odot} = 357.5277233^{\circ} + 35999.05034\ T_{UT1} \tag{2.28}$$

where T_{UT1} is the Julian centuries past J2000

$$T_{UT1} = \frac{JD(Y, M, D, h, m, s) - 2{,}451{,}545}{36{,}525} \tag{2.29}$$

When determining both $\phi_{\odot}$ and $M_{\odot}$ they should be reduced to the range 0° to 360°. With these values the longitude of the ecliptic in degrees is

$$\phi_{ecliptic} = \phi_{\odot} + 1.914666471^{\circ} \sin(M_{\odot}) + 0.019994643 \sin(2M_{\odot}) \tag{2.30}$$

The obliquity of the ecliptic is

$$\varepsilon = 23.439291^{\circ} - 0.0130042\, T_{UT1} \tag{2.31}$$

With the longitude and the obliquity of the ecliptic known the unit vector direction from the Earth to the Sun is then

$$\mathbf{e}_{\oplus\odot} = \begin{bmatrix} \cos(\phi_{ecliptic}) \\ \cos(\varepsilon)\sin(\phi_{ecliptic}) \\ \sin(\varepsilon)\sin(\phi_{ecliptic}) \end{bmatrix} \tag{2.32}$$

The distance between the Earth and the Sun in Astronomical Units (AU) is

$$r_{\oplus\odot} = 1.000140612 - 0.016708617\cos(M_{\odot}) - 0.000139589\cos(2M_{\odot}) \tag{2.33}$$

By converting the spacecraft's position from km to AU the spacecraft's position with respect to the Sun is given by

$$\mathbf{r}_{sat\odot} = \mathbf{r}_{\oplus\odot} - \mathbf{r} \tag{2.34}$$

where the total distance between the Sun and the spacecraft and the corresponding unit vector are

$$\begin{aligned} r_{sat\odot} &= \|\mathbf{r}_{sat\odot}\| \\ \mathbf{e}_{sat\odot} &= \frac{\mathbf{r}_{sat\odot}}{r_{sat\odot}} \end{aligned} \tag{2.35}$$

The pressure due to solar radiation can now be found as

$$P_{\odot} = \frac{\mathcal{F}_{\odot}}{c r_{sat\odot}^2} \tag{2.36}$$

where $\mathcal{F}_\odot \approx 1363$ W/m^2, the solar constant, is the flux density of the solar radiation at a distance of 1 AU from the Sun, and $c = 299,792,458$ m/s is the speed of light. The solar constant can be approximated as the specified value, however, it does vary depending on current solar activity [19].

Because the position vector of the spacecraft and the position vector of the Earth are known it is possible to determine when the spacecraft is in the Earth's shadow. A simplistic approach was used where the Earth's shadow is assumed to be a cylindrical projection of the Earth's diameter along the direction of the Sun to Earth vector [18]. Therefore, the spacecraft is in the Earth's shadow if

$$\mathbf{r} \cdot \mathbf{e}_{\oplus\odot} < -\sqrt{r^2 - R_\oplus^2} \tag{2.37}$$

The total force due to SRP can be written as

$$\mathbf{F}_{\text{SRP}} = \sum_{i=1}^{N} F^i_{r,\text{SRP}}\hat{r} + F^i_{\theta,\text{SRP}}\hat{\theta} + F^i_{h,\text{SRP}}\hat{h} \tag{2.38}$$

From the total force the perturbing acceleration due to SRP in terms of the LVLH frame is

$$\mathbf{f}_{\text{SRP}} = A\frac{\mathbf{F}_{\text{SRP}}}{m} \tag{2.39}$$

The total torque on the spacecraft due to SRP is the summation of the torques experienced by the plates given by

$$\mathbf{L}_{\text{SRP}} = \sum_{i=1}^{N} \mathbf{r}^i \times \mathbf{F}^i_{\text{SRP}} \tag{2.40}$$

2.3.4. Summation of Perturbations. By summing the components of the perturbing accelerations the total f_r, f_θ, and f_h are found to be

$$f_r = f_{r,\tau} + f_{r,J_2} + f_{r,\text{drag}} + f_{r,\text{SRP}} \tag{2.41}$$

$$f_\theta = f_{\theta,\tau} + f_{\theta,J_2} + f_{\theta,\text{drag}} + f_{\theta,\text{SRP}} \tag{2.42}$$

$$f_h = f_{h,\tau} + f_{h,J_2} + f_{h,\text{drag}} + f_{h,\text{SRP}} \tag{2.43}$$

where the τ subscript denotes the acceleration components from the applied thrust. Similarly, the total torque that affects the spacecraft's attitude is

$$\mathbf{L} = \mathbf{L}_\tau + \mathbf{L}_{\text{drag}} + \mathbf{L}_{\text{SRP}} \tag{2.44}$$

It should be noted that this work neglected to include the orbital effects of third-body perturbations such as from the Sun and the Moon, the effect on attitude from J_2, and the torque that would be generated from the existence of a magnetic dipole within the spacecraft.

3. ANALYTIC THRUST DETERMINATION

3.1. TWO-BODY RAAN MANEUVER

The Gauss VOP equations can be integrated over a short time span to estimate the thrust of a spacecraft performing an orbit changing maneuver. This is most easily seen in either Equation 2.3 for the inclination rate of change, or Equation 2.4 for the RAAN rate of change. Based on the results found in Morton [20], this study's author made the choice to focus on the spacecraft performing a RAAN changing maneuver. By making the assumptions that the orbit is circular ($e = 0$), the thrust is constant in direction and magnitude, and the change in inclination is negligible, then the equation for the RAAN rate of change decouples from the other five Gauss VOP equations and can be integrated directly as

$$\begin{aligned}
\int_{\Omega_i}^{\Omega_f} d\Omega &= \int_{t_i}^{t_f} \frac{r f_h \sin\theta}{h \sin i} dt \qquad \text{where} \quad d\theta = \frac{h}{r^2} dt \\
&= \frac{r^3 f_h}{h^2 \sin i} \int_{\theta_i}^{\theta_f} \sin\theta d\theta \\
&= \frac{r^3 f_h}{h^2 \sin i} [-\cos\theta] \Big|_{\theta_i}^{\theta_f} \\
\Omega_f - \Omega_i &= \frac{r^3 f_h}{h^2 \sin i} [\cos\theta_i - \cos\theta_f] \qquad (3.1)
\end{aligned}$$

where the subscripts i and f denote the values at the start and end of the maneuver respectively. The thrust F_h can then be found by solving the equation for f_h the perturbing acceleration in the $\hat{h}$-direction and multiplying by the mass m as

$$\begin{aligned}
f_h = \frac{F_h}{m} &= \frac{(\Omega_f - \Omega_i) h^2 \sin i}{r^3 [\cos\theta_i - \cos\theta_f]} \\
F_h &= \frac{(\Omega_f - \Omega_i) h^2 m \sin i}{r^3 [\cos\theta_i - \cos\theta_f]} \qquad (3.2)
\end{aligned}$$

In this study the mass is assumed to remain constant during the maneuver. Because the mass of propellant expended to perform the maneuver is negligible compared to the total mass of the spacecraft, this is a reasonable assumption.

3.2. TWO-BODY RAAN MANEUVER INCLUDING J_2

Of the perturbations included in the analysis, J_2 is the only perturbation that is strictly dependent on only the orbital position of the spacecraft; atmospheric drag and SRP are also dependent on the attitude of the spacecraft. While atmospheric drag and SRP effects could be included, to do so would require making many assumptions. From a preliminary analysis it was found that at an altitude of approximately 400 km the drag and SRP forces were 10^{-3} and 10^{-4} magnitudes less than the estimated electric mode thrust force along the $\hat{h}$ direction respectively, and were therefore assumed to have a negligible effect on thrust determination. To consider the perturbing acceleration effects due to J_2, the same assumptions were made as before. Now the Gauss VOP equation for the rate of change of RAAN can be integrated as

$$\begin{aligned}\int_{\Omega_i}^{\Omega_f} d\Omega &= \int_{t_i}^{t_f} \frac{r\sin\theta}{h\sin i}(f_{h,\tau} + f_{h,J_2})dt \qquad \text{where} \quad d\theta = \frac{h}{r^2}dt \\ &= \frac{r^3 f_{h,\tau}}{h^2\sin i}\int_{\theta_i}^{\theta_f}\sin\theta d\theta + \frac{r^3}{h^2\sin i}\int_{\theta_i}^{\theta_f} f_{h,J_2}\sin\theta d\theta \end{aligned} \tag{3.3}$$

where $f_{h,\tau}$ is the perturbing thrust acceleration along the $\hat{h}$ direction and f_{h,J_2} is the perturbing J_2 acceleration along the $\hat{h}$ direction.

Because f_{h,J_2} is time varying it cannot be taken out of the integral, however by substituting it for Equation 2.20, Equation 3.3 can be integrated as

$$\begin{aligned}
\int_{\Omega_i}^{\Omega_f} d\Omega &= \frac{r^3 f_{h,\tau}(\cos\theta_i - \cos\theta_f)}{h^2 \sin i} + \frac{r^3}{h^2 \sin i}\int_{\theta_i}^{\theta_f} -\frac{3\mu J_2 R_\oplus^2}{r^4}\left(\cos i \sin i \sin\theta\right)\sin\theta d\theta \\
&= \frac{r^3 f_{h,\tau}(\cos\theta_i - \cos\theta_f)}{h^2 \sin i} - \frac{3\mu J_2 R_\oplus^2 \cos i}{h^2 r}\int_{\theta_i}^{\theta_f} \sin^2\theta d\theta \\
&= \frac{r^3 f_{h,\tau}(\cos\theta_i - \cos\theta_f)}{h^2 \sin i} - \frac{3\mu J_2 R_\oplus^2 \cos i}{h^2 r}\left[\frac{1}{2}(\theta - \sin\theta\cos\theta)\right]_{\theta_i}^{\theta_f} \\
\Omega_f - \Omega_i &= \frac{r^3 f_{h,\tau}(\cos\theta_i - \cos\theta_f)}{h^2 \sin i} - \frac{3\mu J_2 R_\oplus^2 \cos i}{2h^2 r}\left[\theta_f - \sin\theta_f\cos\theta_f - \theta_i + \sin\theta_i\cos\theta_i\right]
\end{aligned}$$

As before the thrust can be found by solving for $f_{h,\tau}$ as

$$\begin{aligned}
f_{h,\tau} = \frac{F_{h,\tau}}{m} &= \frac{h^2 \sin i}{r^3(\cos\theta_i - \cos\theta_f)}\left\{\Omega_f - \Omega_i + \frac{3\mu J_2 R_\oplus^2 \cos i}{2h^2 r}\left[\theta_f - \sin\theta_f\cos\theta_f - \theta_i + \sin\theta_i\cos\theta_i\right]\right\} \\
F_{h,\tau} &= \frac{h^2 m \sin i}{r^3(\cos\theta_i - \cos\theta_f)}\left\{\Omega_f - \Omega_i + \frac{3\mu J_2 R_\oplus^2 \cos i}{2h^2 r}\left[\theta_f - \sin\theta_f\cos\theta_f - \theta_i + \sin\theta_i\cos\theta_i\right]\right\}
\end{aligned} \tag{3.4}$$

3.3. IDEAL ATTITUDE MANEUVER

Another approach to thrust determination is to perform an attitude changing maneuver. By offsetting the thrust line of action from the center of mass the spacecraft can intentionally be slewed and the measured change in angular velocity can be used to determine the an estimate of the thrust. For this maneuver option consider the spacecraft with the body-frame shown in Figure 3.1. For an ideal maneuver the assumption was made that the thrust would be applied in the $b_1 - b_3$ plane, i.e. the thrust would have no offset in the b_2-direction.

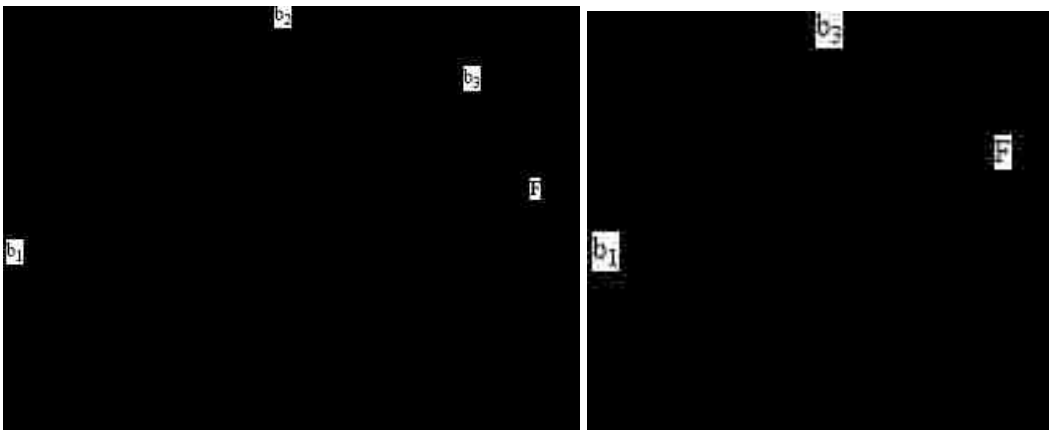

(a) 3-D View (b) Top-down Projection

Figure 3.1. Spacecraft Body Frame Example

The thrust $\mathbf{F} = F\hat{b}_1$ is directed entirely along the $\hat{b}_1$-direction and is offset $-d\hat{b}_1 + \ell\hat{b}_3$ from the origin. The torque is the cross product of the forces vector position from the center of mass (origin for an ideal rectangular prism) and the force vector i.e.

$$\mathbf{L}_\tau = (-d\hat{b}_1 + \ell\hat{b}_3) \times F\hat{b}_1 = \ell F\hat{b}_2 \tag{3.5}$$

For an ideal symmetric rectangular prism-shaped spacecraft the moment of inertia tensor only has moments along the principle axes defined as

$$I = \begin{bmatrix} I_1 & 0 & 0 \\ 0 & I_2 & 0 \\ 0 & 0 & I_3 \end{bmatrix} \tag{3.6}$$

If the angular velocity is defined as, $\boldsymbol{\omega} = \dot{\theta}\hat{b}_2$, then the angular momentum and its rate of change can be written as

$$\mathbf{H} = I\boldsymbol{\omega} \quad \Longrightarrow \quad \mathbf{H} = I_2\dot{\theta}\hat{b}_2 \tag{3.7}$$

$$\frac{d\mathbf{H}}{dt} = \sum \mathbf{L}_\tau \quad \Longrightarrow \quad I_2\ddot{\theta}\hat{b}_2 = \ell F\hat{b}_2 \tag{3.8}$$

By assuming that the thrust is constant Equation 3.8 can be integrated over the duration of the maneuver to determine an estimate of the thrust directly as

$$\int_{t_i}^{t_f} I_2 \ddot{\theta} dt = \int_{t_i}^{t_f} \ell F dt$$

$$I_2[\dot{\theta}(t_f) - \dot{\theta}(t_i)] = \ell F[t_f - t_i]$$

$$F = \frac{I_2[\dot{\theta}(t_f) - \dot{\theta}(t_i)]}{\ell[t_f - t_i]} \tag{3.9}$$

4. ATTITUDE DETERMINATION METHODS

One of the earliest three-axis attitude determination algorithms was Black's TRIAD algorithm [21]. The TRIAD algorithm is a very simple, deterministic method for attitude determination, however, to be deterministic, it must first "discard" a portion of one of the measurements for a solution to be computed.[1] The greatest drawback to the TRIAD algorithm is that it can only incorporate two measurements. For modern spacecraft there are often multiple sensors that can provide measurements for attitude determination including star trackers, Sun sensors, horizon sensors and magnetometers. While more than two measurements could be utilized with the TRIAD algorithm, it would be cumbersome and computationally expensive.

To determine the attitude of a spacecraft using two or more vector measurements and allow weighting of the measurements has commonly been referred to as Wahba's problem [22]. Specifically, Wahba's problem is to find the orthogonal matrix A (i.e., the attitude matrix) that minimizes the loss function

$$\mathcal{L}(A) = \frac{1}{2}\sum_{i=1}^{N} w_i ||\mathbf{b}_i - A\mathbf{r}_i||^2 \tag{4.1}$$

where $\mathbf{b}_i$ are sensor unit vector measurements in terms of the spacecraft's body frame, $\mathbf{r}_i$ are the corresponding unit vector measurements in a reference frame, and w_i are the arbitrary non-negative weights.

[1] Suppose two linearly independent sensor unit vector measurements are known in both the spacecraft body frame and in some reference frame of interest. From the norm constraint each unit vector provides two independent components of scalar attitude information, and only three components of information are required to fully determine the attitude. Therefore, the problem is overdetermined when two measurements are known and one of the components from one of the measurements needs to be "discarded" for a deterministic solution to be computed.

4.1. DAVENPORT'S Q METHOD

The first practical solution to Wahba's problem was Davenport's q method, the solution shown here follows from [23]. Equation 4.1 can be written as

$$\mathcal{L}(A) = -2 \sum_{i=1}^{N} \mathbf{W}_i A \mathbf{V}_i + \text{constant terms} \tag{4.2}$$

where the unnormalized vectors $\mathbf{W}_i$ and $\mathbf{V}_i$ are defined as

$$\mathbf{W}_i = \sqrt{w_i}\mathbf{b}_i \qquad \mathbf{V}_i = \sqrt{w_i}\mathbf{r}_i \tag{4.3}$$

The loss function $\mathcal{L}(A)$ is a minimum when a new modified loss function $\mathcal{L}'(A)$ defined as

$$\mathcal{L}'(A) = \sum_{i=1}^{N} \mathbf{W}_i A \mathbf{V}_i \equiv \text{tr}(W^T A V) \tag{4.4}$$

is a maximum, where the W and V are $3 \times n$ matrices defined by

$$W \equiv \left[\mathbf{W}_1 \vdots \mathbf{W}_2 \vdots \cdots \vdots \mathbf{W}_n \right] \tag{4.5}$$

$$V \equiv \left[\mathbf{V}_1 \vdots \mathbf{V}_2 \vdots \cdots \vdots \mathbf{V}_n \right] \tag{4.6}$$

By substituting Equation 2.13 into Equation 4.4 the modified loss function can be written in terms of the quaternion $\mathbf{q}$ as

$$\mathcal{L}'(A(\mathbf{q})) = \mathbf{q}^T K \mathbf{q} \tag{4.7}$$

where K is a 4×4 matrix given by

$$K = \begin{bmatrix} B + B^T - (\text{tr}B) I_{3x3} & \mathbf{z} \\ \mathbf{z}^T & \text{tr}B \end{bmatrix} \tag{4.8}$$

with the 3×3 matrix B and the vector $\mathbf{z}$ defined as

$$B = \sum_{i=1}^{N} w_i \mathbf{b}_i \mathbf{r}_i^T \tag{4.9}$$

$$\mathbf{z} = \begin{bmatrix} B_{23} - B_{32} \\ B_{31} - B_{13} \\ B_{12} - B_{21} \end{bmatrix} = \sum_{i=1}^{N} w_i (\mathbf{b}_i \times \mathbf{r}_i) \tag{4.10}$$

The best attitude estimate of the spacecraft can then be found by finding the quaternion that maximizes Equation 4.7. By applying the unit norm quaternion constraint of Equation 2.11 through the method of Lagrange multipliers [24], a new gain function $g(\mathbf{q})$ can be defined as

$$g(\mathbf{q}) = \mathbf{q}^T K \mathbf{q} - \lambda \mathbf{q}^T \mathbf{q} \tag{4.11}$$

where λ is the Lagrange multiplier and is chosen such that it satisfies the normalization constraint. By differentiating Equation 4.11 with respect to $\mathbf{q}^T$ and setting the result equal to zero, an eigenvector equation is obtained as

$$\begin{aligned} g(\mathbf{q}) = K\mathbf{q} - \lambda \mathbf{q} = 0 \\ K\mathbf{q} = \lambda \mathbf{q} \end{aligned} \tag{4.12}$$

where λ is an eigenvalue of K and the quaternion that maximizes Equation 4.7 is an eigenvector of K. By substituting Equation 4.12 into Equation 4.7 it can be seen that

$$\mathcal{L}'(A(\mathbf{q})) = \mathbf{q}^T K \mathbf{q} = \mathbf{q}^T \lambda \mathbf{q} = \lambda \tag{4.13}$$

Thus, the best attitude estimate is found when $\mathcal{L}'(A(q))$ is maximized, which is when the quaternion is the eigenvector corresponding to the largest eigenvalue of K.

4.2. QUATERNION ESTIMATOR (QUEST)

While Davenport's q-method was used on some spacecraft, it was unable to provide attitude estimates with adequate frequency for other spacecraft missions, due to the limitations of computers at the time. To compute attitude estimates more frequently Shuster developed the QUEST algorithm, which was first published as the combination of two different papers by Shuster and Oh [25]. To date QUEST has become a widely used method for solving Wahba's problem. The procedure shown to implement QUEST follows from [18].

By defining $\hat{\mathbf{q}}$ as the "optimal" quaternion, then Davenport's eigenvalue condition can be defined as

$$\mathbf{0}_4 = H(\lambda)\hat{\mathbf{q}} \tag{4.14}$$

where

$$H(\lambda) = \lambda I_{4\times4} - K = \begin{bmatrix} (\lambda + \mathrm{tr}B)I_{3\times3} - S & -\mathbf{z} \\ -\mathbf{z}^T & \lambda - \mathrm{tr}B \end{bmatrix} \tag{4.15}$$

and

$$S = B + B^T \tag{4.16}$$

Then Equation 4.14 is equivalent to the equations

$$(\rho I_{3\times3} - S)\hat{\mathbf{q}}_{1:3} = \hat{q}_4\mathbf{z} \tag{4.17}$$

$$(\lambda_{\max} - \mathrm{tr}B)\hat{q}_4 - \mathbf{z}^T\hat{\mathbf{q}}_{1:3} = 0 \tag{4.18}$$

where

$$\rho = \lambda_{\max} + \mathrm{tr}B \tag{4.19}$$

If the largest eigenvalue, $\lambda_{\max}$, were already known, then the optimal quaternion, $\hat{\mathbf{q}}$, would be given as

$$\hat{\mathbf{q}} = \alpha \begin{bmatrix} \text{adj}(\rho I_{3\times 3} - S)\mathbf{z} \\ \det(\rho I_{3\times 3} - S) \end{bmatrix} \tag{4.20}$$

where α is determined by the normalization of $\hat{\mathbf{q}}$. By substituting Equation 4.20 into Equation 4.18 an implicit equation for the maximum eigenvalue is given by

$$(\lambda_{\max} - \text{tr}B)\det(\rho I_{3\times 3} - S) - \mathbf{z}^T \text{adj}(\rho I_{3\times 3} - S)\mathbf{z} = 0 \tag{4.21}$$

which is the characteristic equation of K. An explicit equation for $\lambda_{\max}$ is found by making use of the definitions of the adjoint and the determinate to write

$$\text{adj}(\rho I_{3\times 3} - S) = \text{adj}S + \rho S + \rho(\rho - \text{tr}S) I_{3\times 3} \tag{4.22}$$

$$\det(\rho I_{3\times 3} - S) = \rho^3 - \rho^2 \text{tr}S + \text{tr}(\text{adj}S)\rho - \det S \tag{4.23}$$

The adjoint expression can be further simplified by applying the Cayley-Hamilton Theorem, which states that a constant matrix satisfies its own characteristic equation [26], to the matrix S and after some algebra gives

$$\text{adj}S = S^2 - S\text{tr}S + \text{tr}(\text{adj}S) I_{3\times 3} \tag{4.24}$$

By making these substitutions Equation 4.21 can be written as a quartic equation for λ as

$$\begin{aligned} 0 = \psi(\lambda) = &\left[\lambda^2 - (\text{tr}B)^2 + \text{tr}(\text{adj}S)\right]\left[\lambda^2 - (\text{tr}B)^2 - ||\mathbf{z}||^2\right] \\ &- (\lambda - \text{tr}B)(\mathbf{z}^T S\mathbf{z} + \det S) - \mathbf{z}^T S^2 \mathbf{z} \end{aligned} \tag{4.25}$$

where the largest root of the equation is $\lambda_{\max}$, which can be used to find the optimal quaternion in Equation 4.20.

In this work the QUEST method is used for attitude determination. Sensor measurements were generated for a magnetometer and for multiple Sun sensors on different faces of the spacecraft to ensure that at least two sensors readings would be generated (unless the spacecraft was eclipsed). The magnetometer measurement was generated using the World Magnetic Model shown in Appendix A. It is noted that magnetometer measurements are known to exhibit some inaccuracies due to the secular variations present in the Earth's magnetic model, particularly when measuring the field near the magnetic North and South poles. However, for the inclination considered in this work ($i = 45°$) the magnetometer measurements are believed to provide a reasonably accurate and reliable level of attitude determination throughout the orbit. The Sun sensor measurements were generated using the procedure shown in Section 2.3.3. A complication occurs when the spacecraft is eclipsed because Sun sensor measurements can no longer be generated. In this situation, the most recent attitude state is propagated using Euler's method with one second time intervals until new Sun sensor measurements can be taken.

5. SIMULATION MODEL

The Missouri University of Science and Technology satellite APEX was chosen as a case study to demonstrate the effect attitude has on thrust determination. To accomplish this goal a simulation was designed that imposed specific attitude and orbital requirements before a maneuver could be performed. The attitude requirement was that APEX needed to achieve and maintain its desired attitude state by reducing the magnitude of its angular velocity to less than 10^{-3} rad/s with respect to the ECI frame. The orbital requirement was that the location of the maneuver needed to be centered about $\theta = 90^{\circ}$ to maximize the (small) change in RAAN for thrust determination purposes (to ensure the orbit changes could be accurately sensed by APEX's GPS receiver). Because APEX's launch vehicle and orbit were unknown at the time of this study, an arbitrary set of initial conditions (shown in Table 5.1) were selected based on common low Earth orbits.

Table 5.1. Initial Keplerian Orbital Elements

a (km)	e	i (deg)	Ω (deg)	ω (deg)
6787.072	0.005	45	45	90

Along with the orbital elements, an arbitrary initial attitude quaternion and quaternion rate were chosen as

$$\mathbf{q}(t_0) = \begin{bmatrix} -0.134165 \\ 0.300859 \\ -0.079953 \\ 0.940792 \end{bmatrix} \qquad \dot{\mathbf{q}}(t_0) = \begin{bmatrix} 0.057665 \\ 0.043415 \\ 0.022068 \\ -0.003784 \end{bmatrix} \tag{5.1}$$

where the quaternion rate was calculated using an initial angular velocity of 3 deg/s along each body frame axis. This angular velocity was based off of expected tip-off rates when deployed from a CubeSat dispenser [27].

To reach and maintain a desired attitude can be achieved through the use of actuators, which are used to drive the attitude rate to near zero. The most commonly used actuators are thrusters, reaction wheels, control moment gyros, and magnetorquers. Of these potential actuators, APEX will likely have reaction wheels and magnetorquers for attitude control, however for this study only reaction wheels were considered. Because reaction wheels are an angular momentum transfer device, there is a maximum amount of angular momentum they are able to store before they saturate. Without another type of actuator to dissipate the stored momentum, control of the spacecraft can be lost once the reaction wheel reaches its saturation state. In this study the reaction wheels were assumed to never saturate.

5.1. REACTION WHEEL CONTROL LAW

To know if the spacecraft has reached the desired attitude state, $\mathbf{q}_c$, an error quaternion, δq, can be defined as

$$\delta\mathbf{q} = \mathbf{q} \otimes \mathbf{q}_c^{-1} \tag{5.2}$$

This makes use of the quaternion multiplication property where a quaternion multiplied by the inverse of itself will be equal to the identity quaternion. Therefore when the error quaternion equals the identity quaternion the desired attitude state has been achieved. However, to maintain the desired attitude the angular velocity of the spacecraft must be driven towards zero. This can be done by defining a feedback control law for reaction wheel torques such as [18]

$$\bar{\mathbf{L}} = -k_p \text{sign}(\delta q_4)\boldsymbol{\delta q}_{1:3} - k_d\boldsymbol{\omega} \tag{5.3}$$

where k_p and k_d are positive gains. Because attitude quaternions are not unique the possibility exists for a "short" and a "long" path to the desired attitude state. However, by multiplying the error quaternion by the sign of its scalar component it can be ensured that the control law will always take the shortest path to reach the desired attitude state. The stability of the feedback control law in Equation 5.3 is proven in [18] by defining the

Lyapunov function

$$V = \frac{1}{4}\boldsymbol{\omega}^T J\boldsymbol{\omega} + \frac{1}{2}k_p\boldsymbol{\delta q}_{1:3}^T\boldsymbol{\delta q}_{1:3} + \frac{1}{2}k_p(1-\delta q_4)^2 \geq 0 \tag{5.4}$$

where it is shown that $\dot{V} \leq 0$, proving the closed-loop system is stable.

By considering the perturbing torques discussed in Section 2 and the reaction wheel control law, from [18] the rotational dynamics of the spacecraft can be represented as

$$J\dot{\boldsymbol{\omega}} = -[\boldsymbol{\omega}\times]J\boldsymbol{\omega} + \bar{\mathbf{L}} + \mathbf{L}_\tau + \mathbf{L}_{\text{drag}} + \mathbf{L}_{\text{SRP}} \tag{5.5}$$

$$\dot{\mathbf{h}} = -[\boldsymbol{\omega}\times]\mathbf{h} - \bar{\mathbf{L}} \tag{5.6}$$

where $\mathbf{L}_\tau$, $\mathbf{L}_{\text{drag}}$, and $\mathbf{L}_{\text{SRP}}$ are perturbing torques, $\bar{\mathbf{L}}$ is an effective reaction wheel torque input, J is the spacecraft's inertia tensor, $\dot{\mathbf{h}}$ is the reaction wheel torque, $\mathbf{h}$ is the reaction wheel's angular momentum, and $[\boldsymbol{\omega}\times]$ is a skew-symmetric matrix of the spacecraft's angular velocity represented as

$$[\boldsymbol{\omega}\times] = \begin{bmatrix} 0 & -\omega_3 & \omega_2 \\ \omega_3 & 0 & -\omega_1 \\ -\omega_2 & \omega_1 & 0 \end{bmatrix} \tag{5.7}$$

By propagating the rotational dynamics model of APEX given by Equations 5.5 and 5.6 a truth state for the attitude can be acquired.

5.2. SIMULATION PROCESS

The simulation was created entirely in MATLAB. The built-in function ode113 was used to numerically integrate the Gauss VOP equations (2.2-2.6) and APEX's rotational dynamics (5.5, 5.6) with an absolute error tolerance of 10^{-14} and a relative error tolerance of

10^{-12}. For each simulation it was assumed that APEX receives a perfect GPS measurement at one second intervals, therefore APEX was able to perfectly know its position, velocity, and Keplerian elements.

When performing a RAAN changing maneuver APEX's ideal body frame to LVLH frame attitude matrix is

$$A_{ideal} = \begin{bmatrix} 0 & 1 & 0 \\ 0 & 0 & 1 \\ 1 & 0 & 0 \end{bmatrix} \tag{5.8}$$

this attitude aligns APEX's body frame such that the thrust is entirely directed along the LVLH frame $\hat{h}$-direction and has the GPS antenna pointed away from the Earth (so that it always receives a signal). To begin to determine the effects of imperfect attitude control on thrust determination, the desired attitude state was rotated about the $\hat{r}$-axis of the LVLH frame, as shown in Figure 5.1 and Equation 5.9. This redirects the thrust from being entirely along the $\hat{h}$-direction of the LVLH frame to being offset by an angular amount α, so that the change in RAAN is no longer being maximized.

$$A_{des} = \begin{bmatrix} 1 & 0 & 0 \\ 0 & \cos\alpha & \sin\alpha \\ 0 & -\sin\alpha & \cos\alpha \end{bmatrix} A_{ideal} \tag{5.9}$$

Therefore, the angle α is the attitude pointing error from the ideal body frame alignment. The desired attitude matrix A_{des} is the attitude that the control law is driving the state towards. Because the controller is unaware of the angle α, the controller always "thinks" that it is driving the system to the ideal attitude A_{ideal}, when it is actually driving the system to the rotated attitude A_{des}. For example when $\alpha = 15°$ the controller will try to maintain an angular offset of 15° about the $\hat{r}$-axis of the LVLH frame for the entire simulation. This angular offset also results in the thrust acceleration term, $f_{\tau,\theta}$, being nonzero, which will have an effect on all of the orbital elements as can be seen in the Gauss variation of

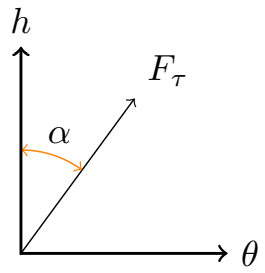

Figure 5.1. Thrust Angular Offset

parameters (Equations 2.2-2.6). The rotation about the $\hat{r}$-axis was arbitrarily selected as an initial study into how imperfect attitude determination effects thrust determination. It is acknowledged that attitude error will be exhibited along all three axes with the errors also time-varying, and that further research should be done to include such cases.

Another consideration to account for is that the thruster is aligned with the geometrical centroid of APEX ($x = y = z = 0$), while the center of mass of the prototype APEX is located at

$$\mathbf{X}_{CM} = \begin{bmatrix} 2.184 \\ -1.538 \\ 16.558 \end{bmatrix} \text{ mm} \tag{5.10}$$

in its current prototype configuration. Because the thruster is not aligned with the center of mass this will create a small torque bias that will rotate APEX away from its desired attitude. The effects of this bias torque on the thrust determination can be seen in the results for the true attitude state.

However, when on-orbit a spacecraft will not know its true attitude, it will only able to estimate its attitude through sensor readings. Therefore, it is useful to quantify the effects the attitude determination system has on thrust determination. To do this the simulation using the true attitude was modified to use the QUEST algorithm. To verify the accuracy of the QUEST algorithm, the sensor measurements were first generated without noise. By

not including noise the system is expected to perform very similar to when using the true attitude. Then by adding noise to the sensor measurements, the effects of the accuracy of the attitude determination system can be evaluated. A flow chart outlining the simulation process is provided in Figure 5.2.

A partial verification of the MATLAB simulation was performed using Systems Tool Kit (STK) and is shown in Appendix B. For the verification the simulations were performed with perfect pointing for the entire maneuver, by making the assumption that the thrust would be acting through the center of mass of APEX. The only perturbation considered in the verification was the effect of the zonal harmonic J_2 on the orbital elements.

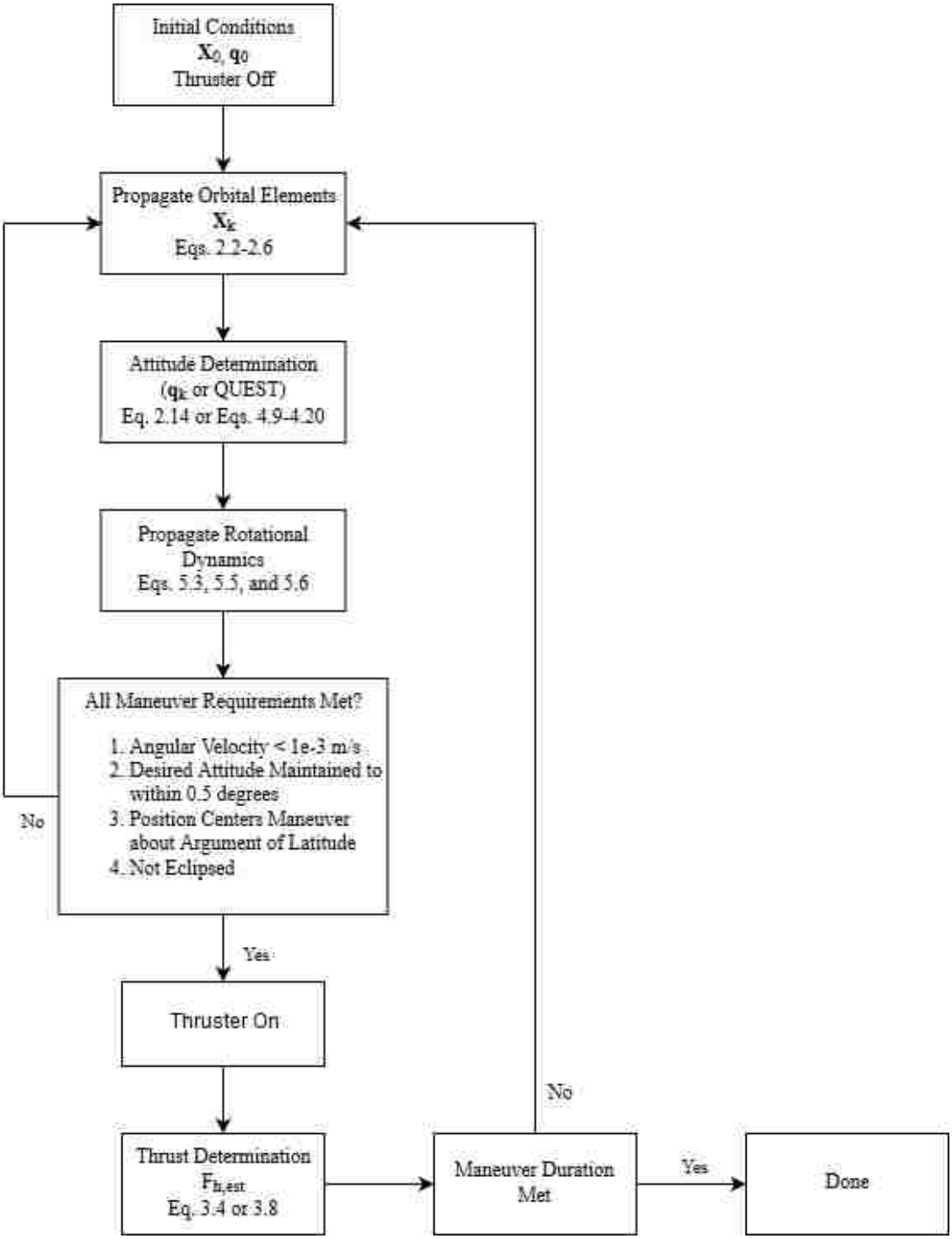

Figure 5.2. Simulation Flow Chart

6. RESULTS AND DISCUSSION

6.1. RAAN CHANGING MANEUVER

The RAAN-changing maneuver was designed to integrate with the concept of operations for the APEX mission. Hence, after launch vehicle deployment APEX begins in a tumbling state and moves along its orbit until it has reduced its angular velocity to near zero and has reached its desired attitude state with near zero error. A RAAN-changing maneuver is then performed (i.e., numerically simulated) centered about an argument of latitude (θ) of 90° where the direction of the thrust is determined from the true attitude state or the estimated attitude from QUEST. Maneuver durations of 5 seconds and 1500 seconds were chosen for the chemical and electric modes respectively. During the maneuver the analytic thrust determination method given in Section 3.2 is performed at every integration interval (1 second intervals) to estimate the $\hat{h}$ component of the thrust, $F_{h,\text{est}}$. In the simulations the true thrust's magnitude was held constant and its direction in terms of the LVLH frame could be determined by

$$\mathbf{F}_{\text{true}} = A_{true}\mathbf{F}^{B}_{true} = A_{true}\begin{bmatrix} F\hat{b}_1 \\ 0 \\ 0 \end{bmatrix} \tag{6.1}$$

where A_{true} is the true attitude matrix for the rotation from the body frame to the LVLH frame and $\mathbf{F}^{B}_{true}$ is the true body frame thrust vector. A_{true} is based on the initial quaternion and is propagated at every integration interval, the only time it is known by APEX is in the true attitude simulation. The error in the thrust estimate was taken with respect to the true thrust's $\hat{h}$ component as

$$Percent\ Error = \frac{F_{h,\text{est}} - F_{h,\text{true}}}{F_{h,\text{true}}} \times 100\%$$

where a negative percent error denotes that the estimated thrust is less than the true thrust. All of the figures for the thrust estimates begin with one second having elapsed since the thruster began producing a force. The decision to omit the zero thrust value at the zero seconds elapsed point was made to better show to scale the small changes in the values of the thrust estimate.

6.1.1. True Attitude Results. In this section the results shown are for the case where the simulation was run with APEX perfectly knowing its "truth" attitude state. This method shows the effect the attitude has on performing thrust determination, independent of attitude determination errors. For this simulation the spacecraft was rotated away from the desired pointing to replicate imperfect active attitude control.

6.1.1.1. Chemical mode (high thrust, 0.25 N). The chemical mode maneuver is able to very accurately estimate the thrust of APEX because for this mode the change in RAAN is larger and is easier for the system to detect. Surprisingly, as the initial α angle increases and the desired pointing rotates further away from the $\hat{h}$-direction the error in the thrust estimate decreases, as shown in Figure 6.2. This is likely due to the method for thrust determination overestimating the thrust produced during the maneuver, which is believed to be caused by the J_2-induced variations in the Keplerian elements, especially inclination. Figure 6.1 shows that as the maneuver continues the estimate for the thrust decreases. The thrust estimate decreases as the maneuver continues because the angle α increases due to the disturbing torque from the thruster not being perfectly aligned with the spacecraft center of mass, and is shown in Figure 6.3 for the initial $\alpha = 0°$ case. As the maneuver continues the thrust rotates away from the $\hat{h}$-direction of the LVLH frame. This same change in the angle α is present for all of the initial α values. Despite this rotation away from the ideal $\hat{h}$-direction, for all of the initial α angles considered the estimate for the thrust is expected to be within 0.14% of the true thrust. For the high thrust of the chemical mode imperfect attitude appears to have little to no effect on performing thrust determination when the true attitude state is known.

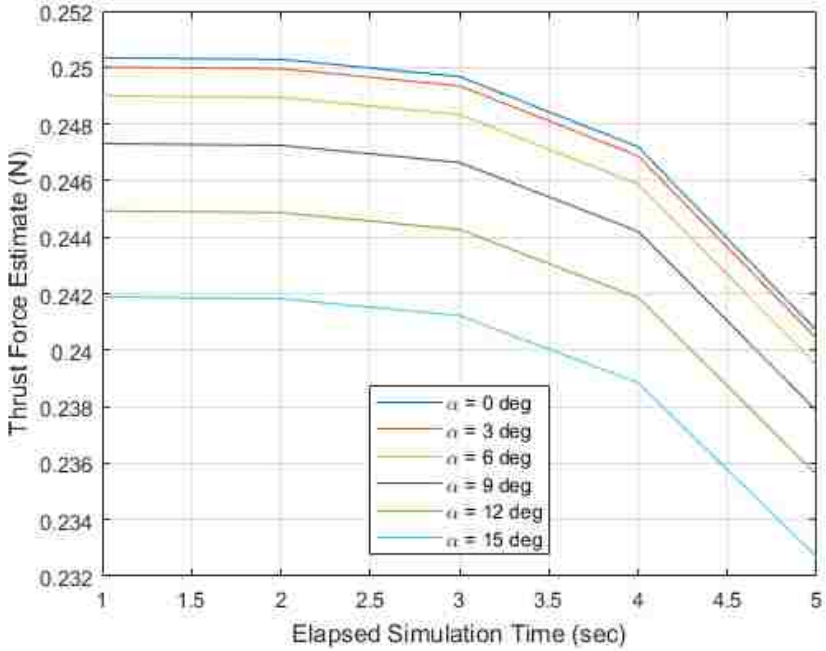

Figure 6.1. Thrust Estimates for Chemical Mode using True Attitude

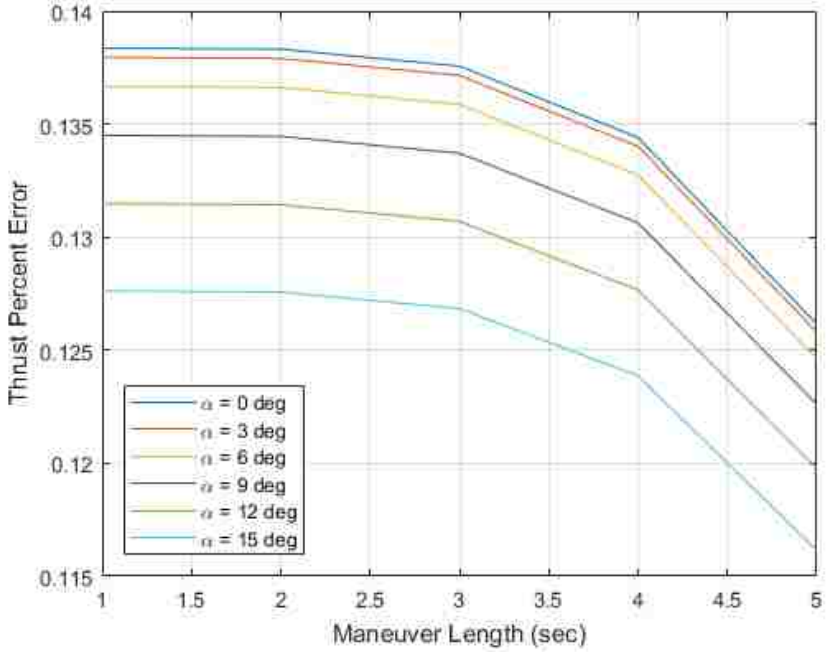

Figure 6.2. Thrust Percent Errors for Chemical Mode using True Attitude

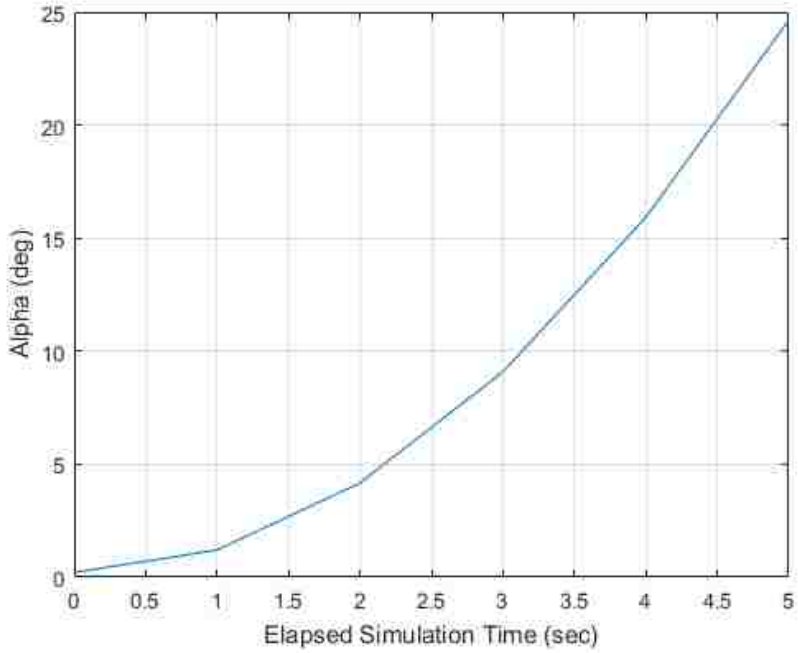

Figure 6.3. Change in the Angle α During Chemical Mode

6.1.1.2. Electric mode (low thrust, 0.25 mN). As expected, for the electric mode as the initial α angle value increases the error in the thrust estimate also increases. Because the thrust for this maneuver is magnitudes smaller than the chemical mode it requires a much longer maneuver duration to measure a change in RAAN. An issue with a longer maneuver is that the measurement is also affected by the J_2-induced secular variations in RAAN, as evident in Figure 6.5. As the maneuver continues the estimate for the thrust increases to a maximum after 705 seconds have elapsed. At this maximum is where the largest error in thrust estimation occurs with the error being 55.66% for the $\alpha = 0°$ case and 57.62% for the $\alpha = 15°$ case. Among the range of α angles considered the difference in error does not exceed 3% at any point. Figure 6.7 shows the change in α over the duration of the maneuver for the initial $\alpha = 0°$ case. An interesting aspect is that the control law is able to return APEX to a stable attitude despite the disturbing torque from the thrust misalignment. However, this stable attitude is not the desired attitude, as it converges to an

α value of approximately 4.715°. This is believed to be due to a limitation in the amount of torque that the reaction wheels are able to generate. By using this method for control, more error is being introduced to the thrust determination. Therefore, a new method for control should be considered to reduce these errors. From these results it can be concluded that if the true attitude is known then the effects of having an imperfect attitude will be small.

While the effects of having an imperfect attitude may be small, the general error in thrust determination for the electric mode is large. To ensure that this error was not due to the assumptions made when deriving Equation 3.4 for analytic thrust determination, a simulation was ran for the electric mode about $\theta = 90°$ where the thrust estimate was also found by numerically integrating Equation 3.3. By numerically integrating the thrust the assumptions made to derive the equation were effectively removed and a comparison of the two methods could be performed. This comparison of the two methods for determining thrust can be seen in Figure 6.4, where it is shown that the thrust is near identical for the two methods. This shows that the assumptions are not the cause of the error and that Equation 3.4 is a valid method for determining the thrust.

After showing that the error was not due to the assumptions made in deriving the thrust equation, it was believed to be caused by the variations in RAAN and it was then of interest to see how RAAN changes over the duration of the entire simulation. Figure 6.8 shows the change in RAAN and argument of latitude, where the vertical dashed-lines denote the start and the end of the maneuver when it is centered about $\theta = 90°$. This shows that by centering the maneuver about $\theta = 90°$ the maneuver is also centered about the largest changes in RAAN due to the secular variations caused by J_2. From the previous results, it was concluded that the performance of the thrust estimate for the electric mode might be improved by moving the location of the maneuver to a section where RAAN plateaus in Figure 6.8. These plateaus in the secular variations in RAAN are located at the ascending node $\theta = 0°$ and the descending node $\theta = 180°$.

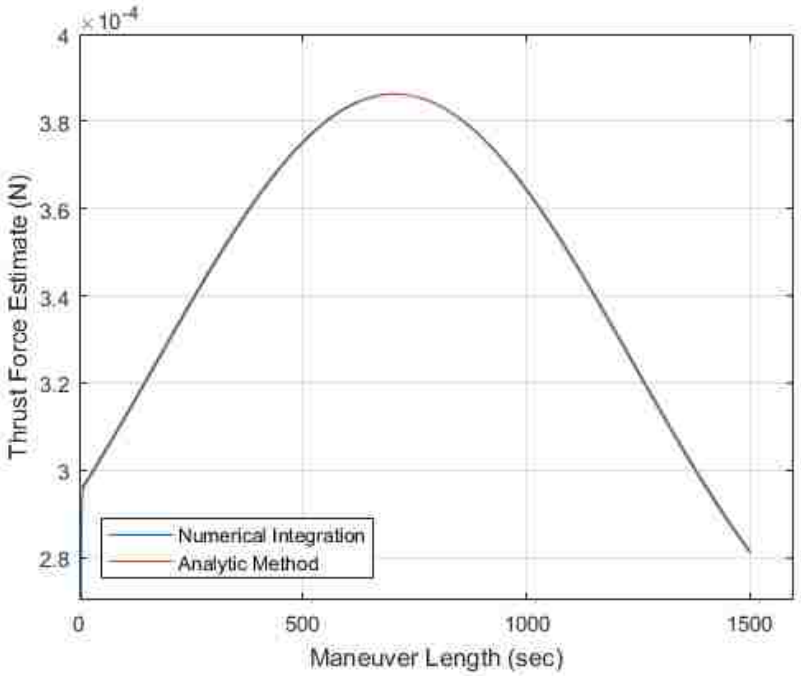

Figure 6.4. Comparison of Analytic Method and Numerically Integrating to Solve for Thrust

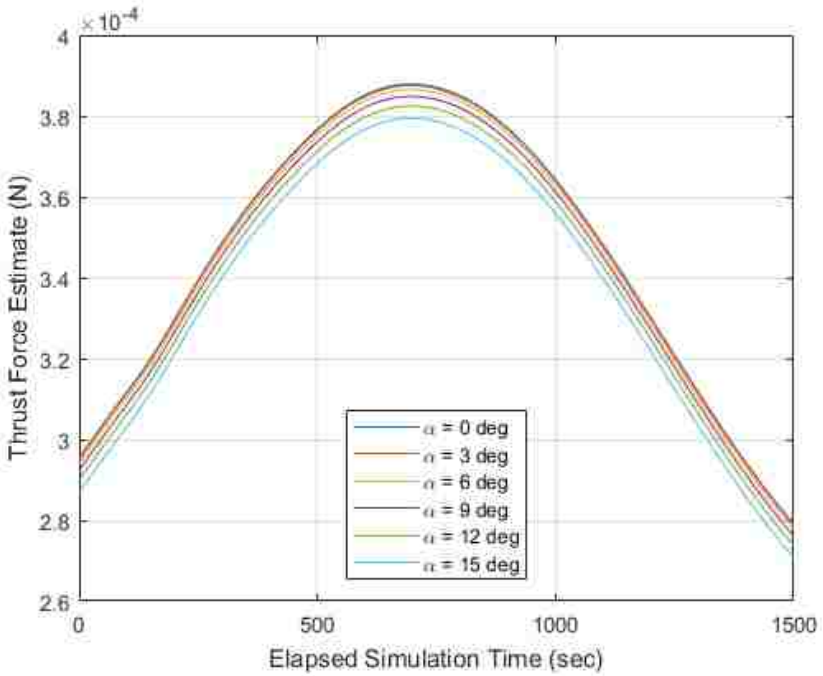

Figure 6.5. Thrust Estimates for Electric Mode using True Attitude Centered about $\theta = 90°$

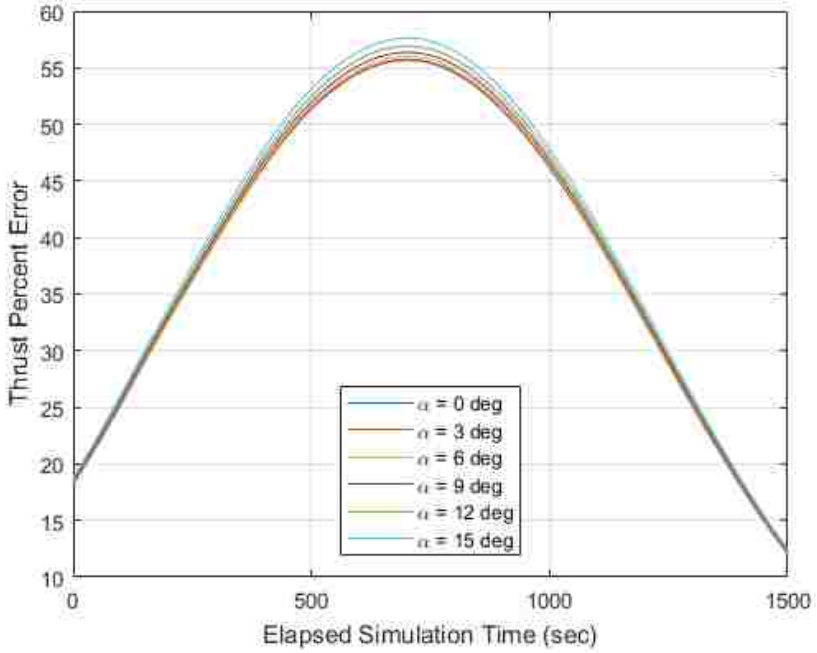

Figure 6.6. Thrust Percent Errors for Electric Mode using True Attitude Centered about $\theta = 90°$

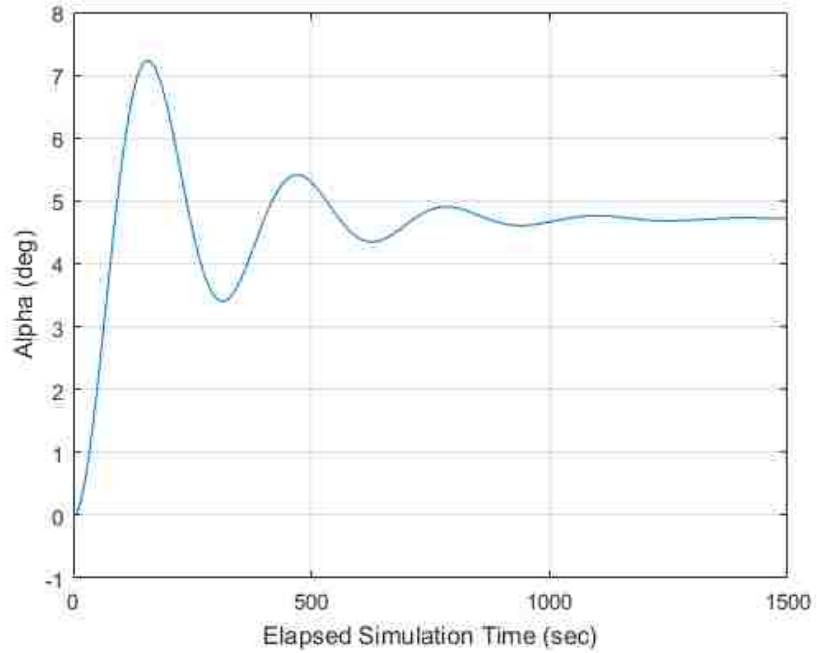

Figure 6.7. Change in the Angle α During Electric Mode

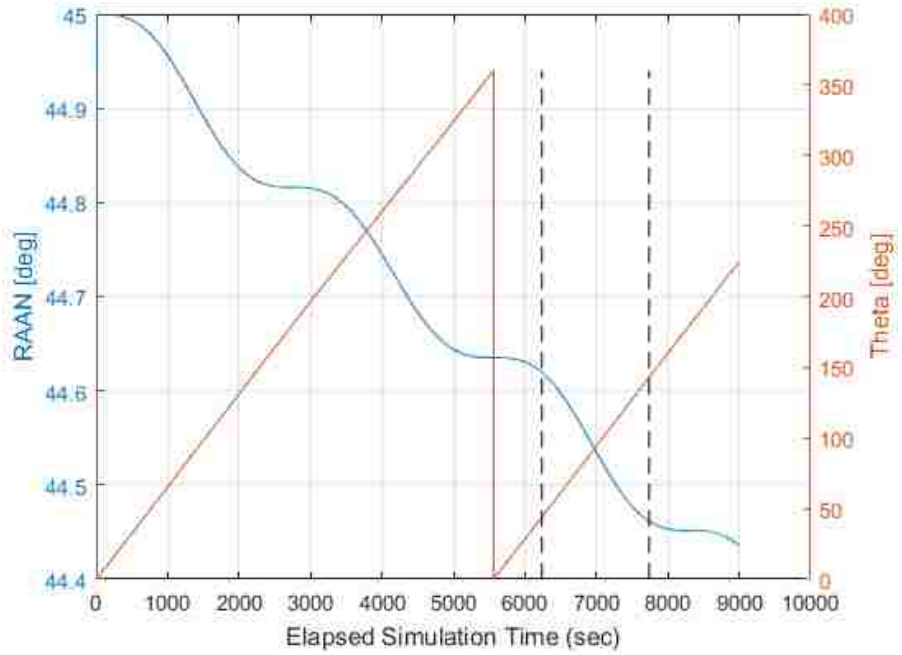

Figure 6.8. Change in RAAN (Ω) and Argument of Latitude (θ) over the Entire Simulation

For this study it was chosen that the simulation maneuver would be centered about the location of the descending node $\theta = 180°$. As shown in Figures 6.9 and 6.10 the performance of the thrust determination improved by a significant amount. For this maneuver the maximum error seen was ±25%, this error is less than half of the error for the maneuver centered about $\theta = 90°$. Also it can be seen that the error caused by having an imperfect attitude had less of an effect when the maneuver location was moved, that among the range of α angles considered the error in thrust was within 1% for all cases.

6.1.2. QUEST Attitude Estimate Results. In this section results are presented for cases where the thrust determination was performed using QUEST attitude estimates with no sensor measurement uncertainty to test the accuracy of the method. At this point another requirement was defined that a maneuver could only occur if the spacecraft was not eclipsed. This was necessary because if the spacecraft was eclipsed the Sun sensors could not take measurements and QUEST would be unable to estimate the attitude.

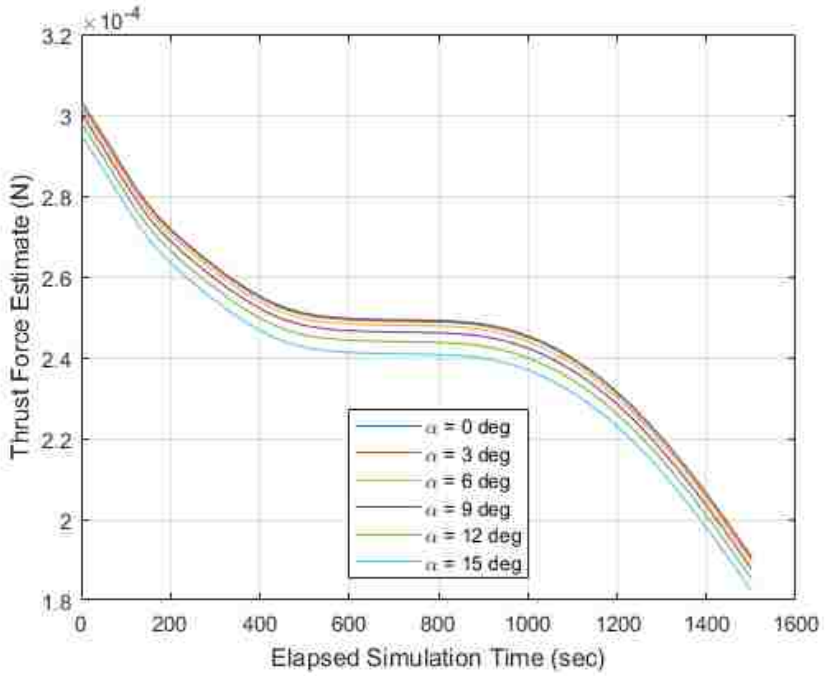

Figure 6.9. Thrust Estimates for Electric Mode using True Attitude Centered about $\theta = 180°$

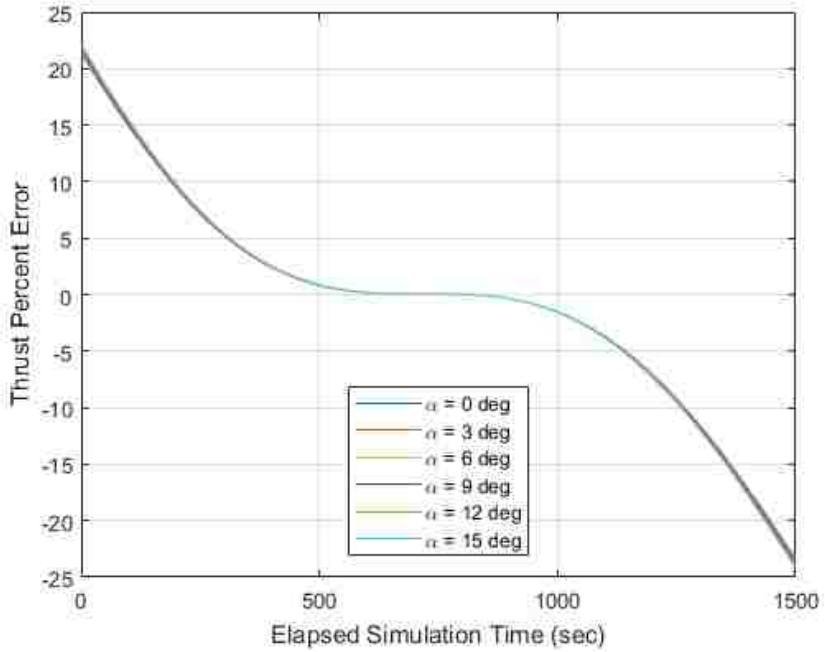

Figure 6.10. Thrust Percent Errors for Electric Mode using True Attitude Centered about $\theta = 180°$

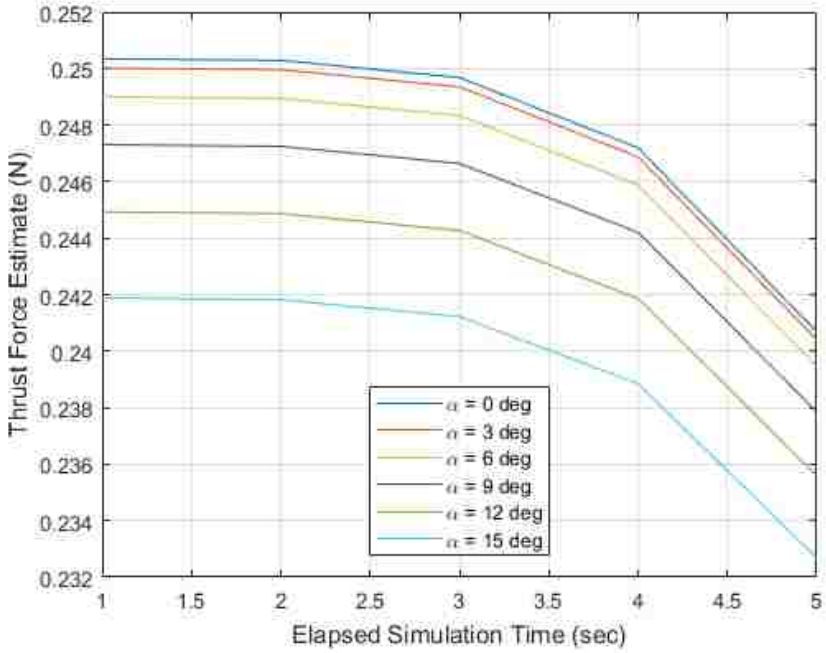

Figure 6.11. Thrust Estimates for Chemical Mode using QUEST

6.1.2.1. Chemical mode (high thrust, 0.25 N). As expected, when the sensor measurements have no measurement uncertainty the system performs nearly identically to the true attitude simulation because the errors in attitude determination are near-zero.

6.1.2.2. Electric mode (low thrust, 0.25 mN). As in the case of the chemical mode, the electric mode results are nearly identical to the simulation using the true attitude for the maneuver centered about $\theta = 90°$ and $\theta = 180°$. Having the same results as the truth method verifies the accuracy of using QUEST as an attitude determination system.

6.1.3. QUEST Attitude Estimate Results with Uncertainty. The results presented in this section include sensor measurements for the magnetometer and the Sun sensors with noise added to make the simulation more realistic. The noise was added to every measurement the sensors took during the simulation with standard deviations of

$$\sigma_{\text{mag}} = 1667 \text{ nT} \qquad \sigma_{\text{sun}} = 1 \text{ deg}$$

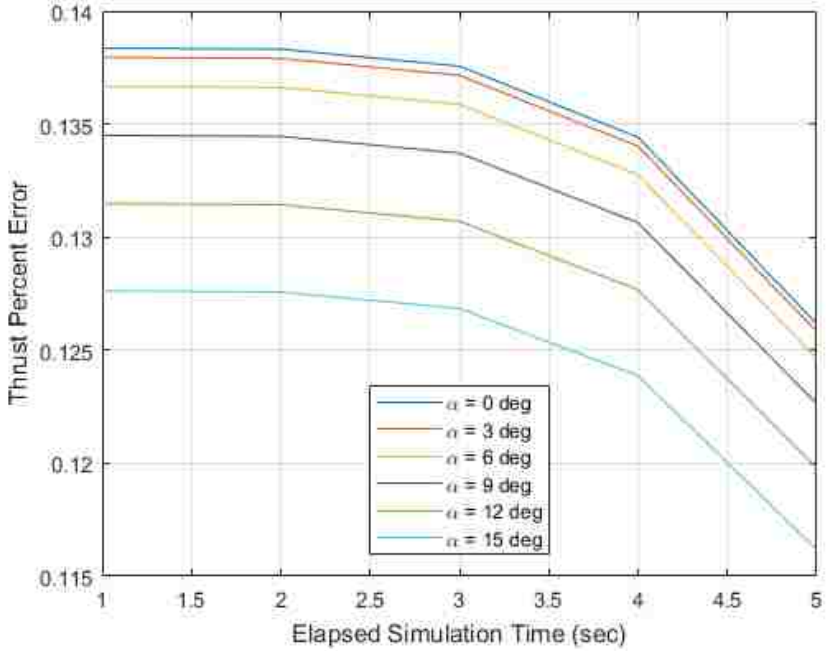

Figure 6.12. Thrust Percent Errors for Chemical Mode using QUEST

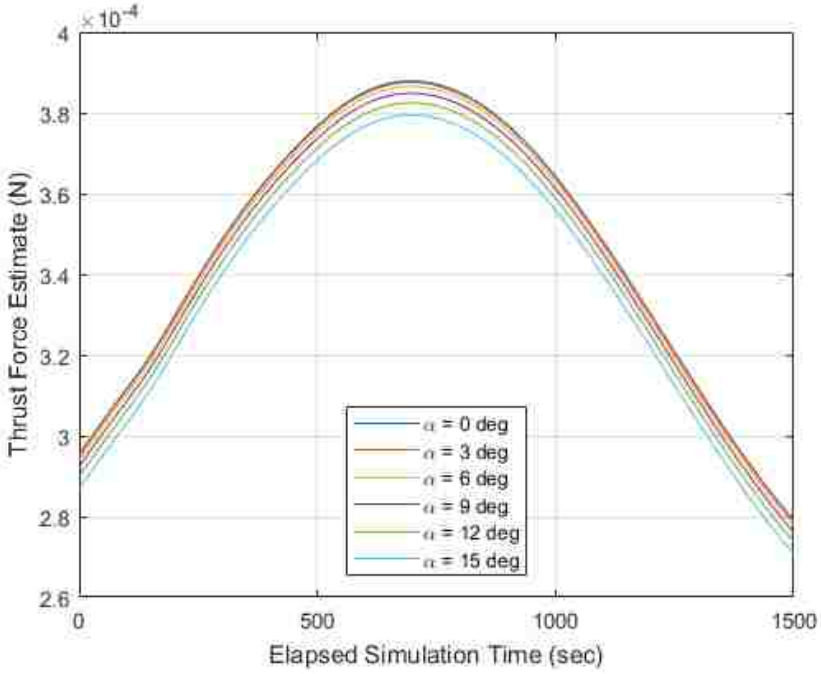

Figure 6.13. Thrust Estimates for Electric Mode using QUEST Centered about $\theta = 90°$

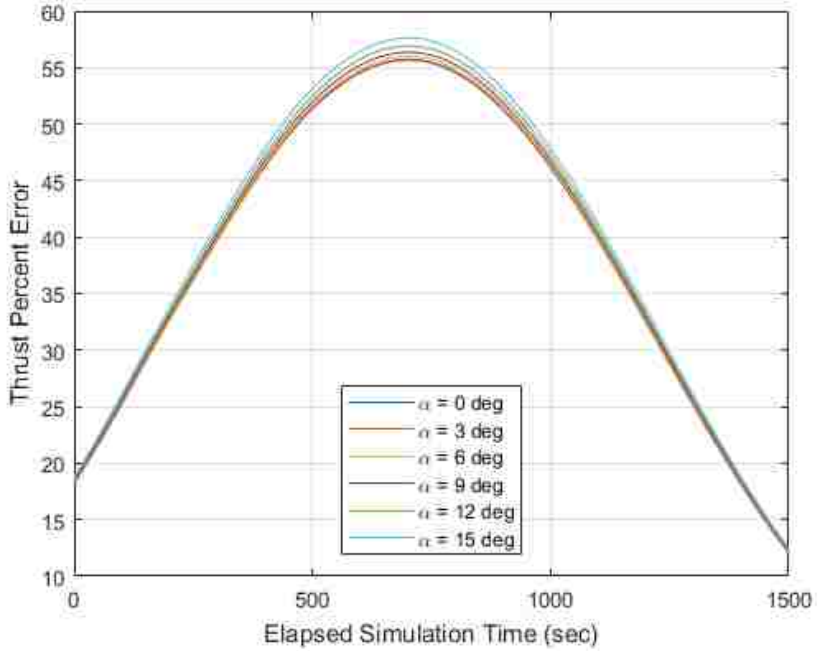

Figure 6.14. Thrust Percent Errors for Electric Mode using QUEST Centered about $\theta = 90°$

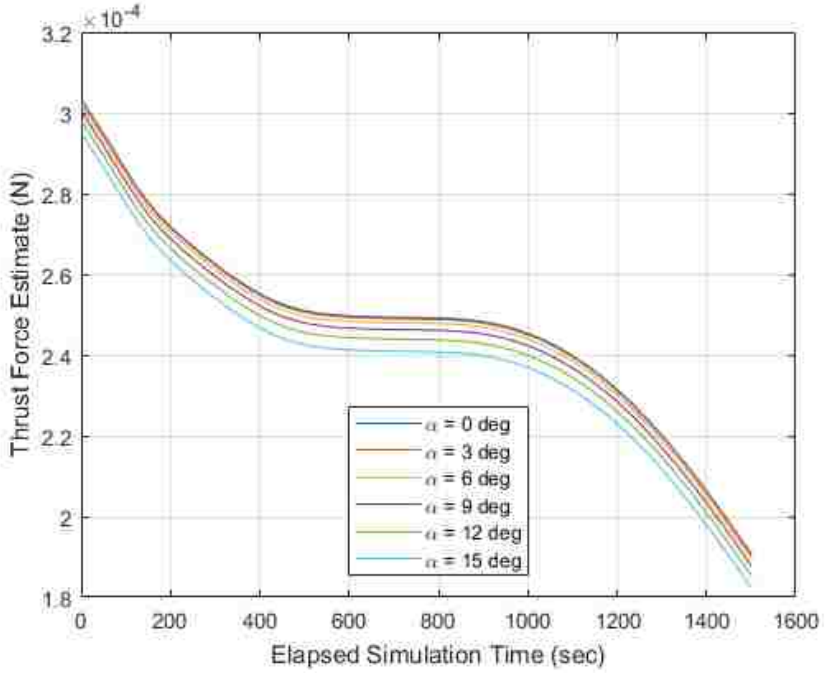

Figure 6.15. Thrust Estimates for Electric Mode using QUEST Centered about $\theta = 180°$

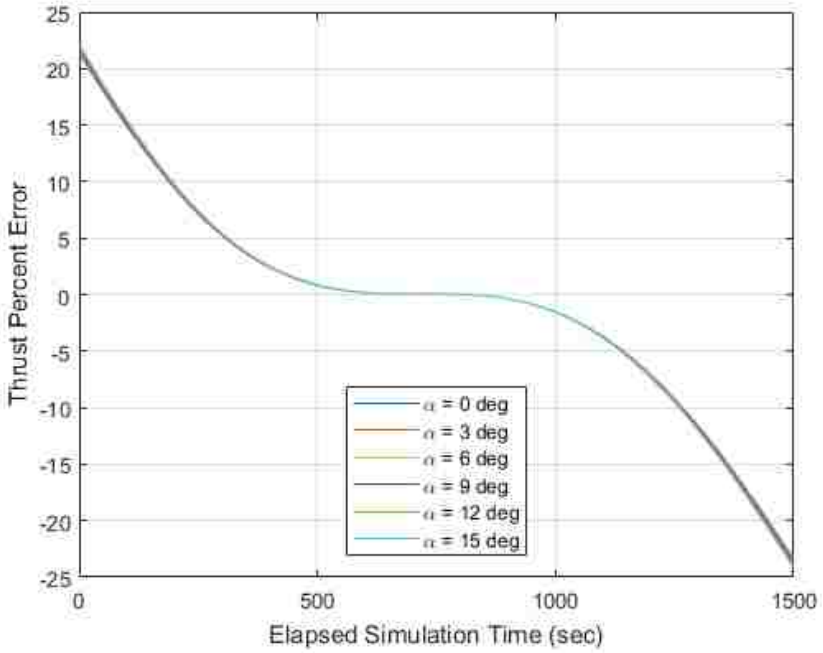

Figure 6.16. Thrust Percent Errors for Electric Mode using QUEST Centered about $\theta = 180°$

The standard deviations were chosen as slightly larger than typical noise values for common CubeSat sized sensors to emphasis the effect attitude determination has on performing thrust determination. The simulation was then run with QUEST using the noisy measurements to estimate the attitude of the spacecraft. This estimated attitude was used in the control law to approach the desired attitude and for the propagation of the orbital elements in the Gauss VOP equations during the maneuver. As with the simulation without uncertainty the additional requirement of the maneuver only being performed when not eclipsed was used.

6.1.3.1. Chemical mode (high thrust, 0.25 N). Adding sensor measurement uncertainty had a significant impact on the results for the chemical mode maneuver. Figure 6.17 shows that the estimate for the thrust is more variable when the measurement uncertainty is included. However, the thrust still follows the same trend as the simulation without measurement uncertainty. The chemical mode thrust determination error is less than ±3% for all cases considered as shown in Figure 6.18.

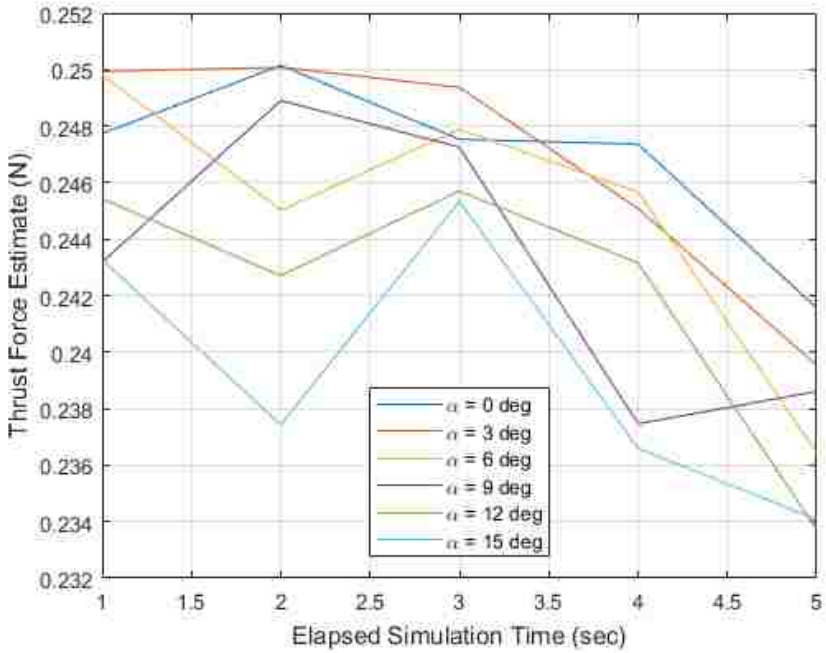

Figure 6.17. Thrust Estimates for Chemical Mode using QUEST with Measurement Uncertainty

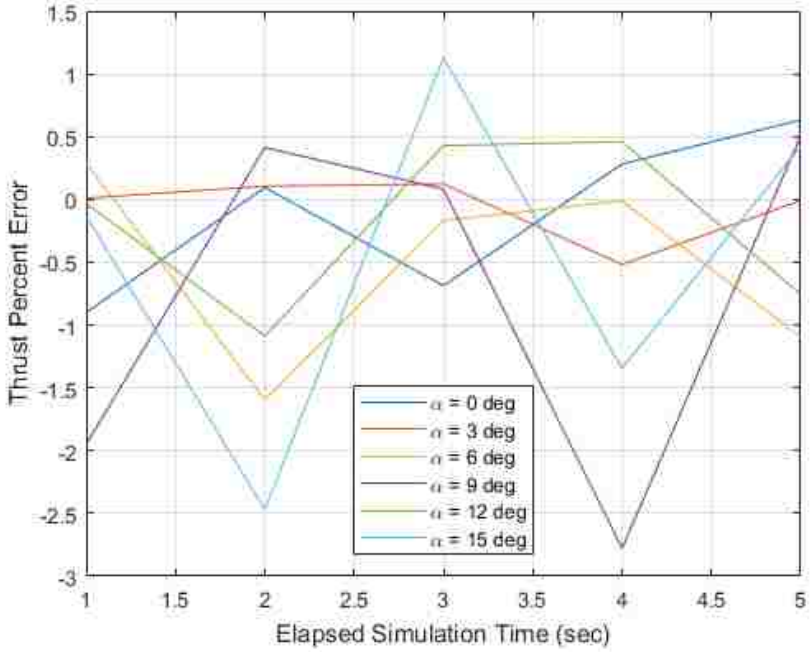

Figure 6.18. Thrust Percent Errors for Chemical Mode using QUEST with Measurement Uncertainty

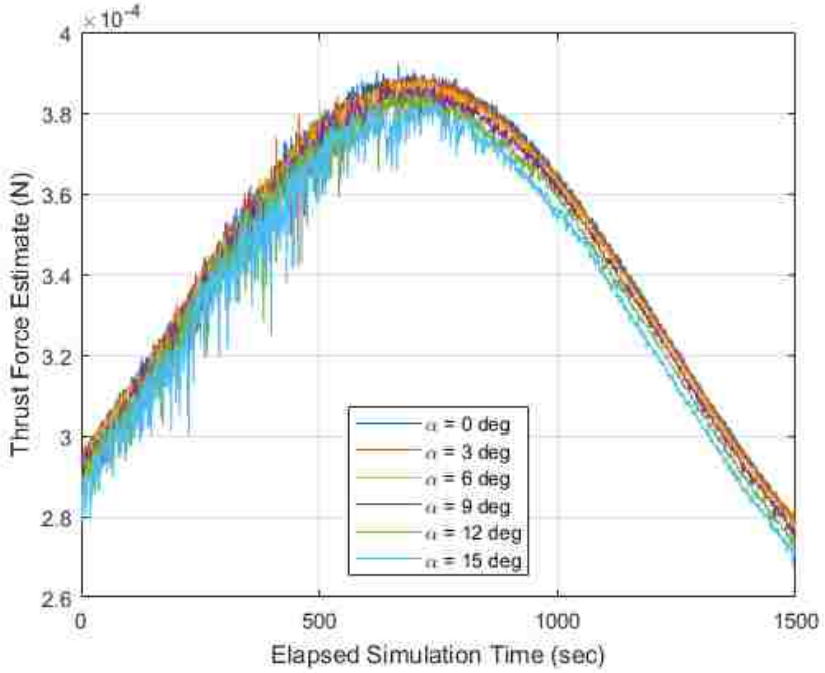

Figure 6.19. Thrust Estimates for Electric Mode Maneuver using QUEST with Measurement Uncertainty Centered about $\theta = 90°$

6.1.3.2. Electric mode (low thrust, 0.25 mN). As expected the estimate for the thrust followed the same trend as the simulation with no measurement uncertainty. As before the simulation was run with the maneuver centered about $\theta = 90°$ and $\theta = 180°$ to determine if adding noise would have the same effect on both maneuver locations. It is shown in Figure 6.20 that adding the noise had the greatest effect during the first 500 seconds of the simulation. For the different cases as the rotation from the $\hat{h}$-direction increases so does the amount the thrust estimate varies. As an example, for the $\alpha = 0°$ rotation case the thrust percent error varies within 6% between time-steps, whereas for the $\alpha = 15°$ rotation it varies up to 10% between time-steps at the beginning of the maneuver. At the end of the maneuver the thrust percent error varies by less than 2% for all cases.

For the maneuver centered about $\theta = 180°$ the error caused by attitude determination noise does decrease. Surprisingly, the variation in the error shows the opposite effect from the maneuver centered about $\theta = 90°$. At the beginning of the maneuver the error varies by

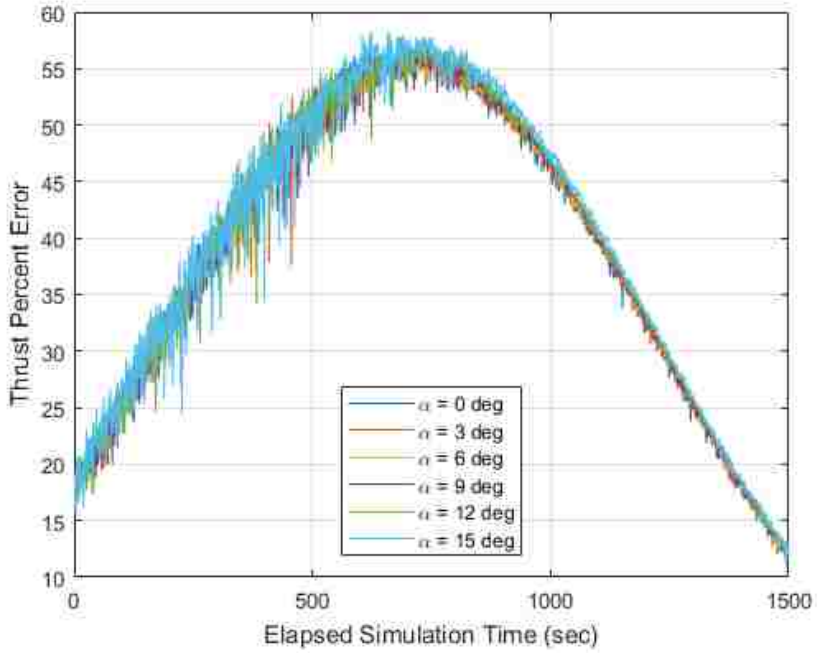

Figure 6.20. Thrust Percent Errors for Electric Mode Maneuver using QUEST with Measurement Uncertainty Centered about $\theta = 90°$

less than 1.5% for all cases. As the maneuver continues the errors caused by noise increase, for the ideal $\alpha = 0°$ case the error varies by 2% whereas for the worst $\alpha = 15°$ case the error varies by 6%. A possible reason for this error is from the sensor readings of the magnetometer, that the secular variations in the Earth's magnetic field are greater at those locations increasing the total error.

6.1.4. Summary. From the results, it can be concluded that having an imperfect attitude has a small effect on performing thrust determination for a RAAN changing maneuver. For the chemical mode when the true attitude is known the percent error was surprisingly largest for the ideal case, $\alpha = 0°$, though for all cases the percent error was less than 0.14%. For the electric mode case having an imperfect attitude had a larger effect though it was also dependent on where the maneuver was centered. When the maneuver was centered about $\theta = 90°$ the percent error was at most 4% larger for the $\alpha = 15°$ case than for the ideal case $\alpha = 0°$, and when it was centered about $\theta = 180°$ the percent error

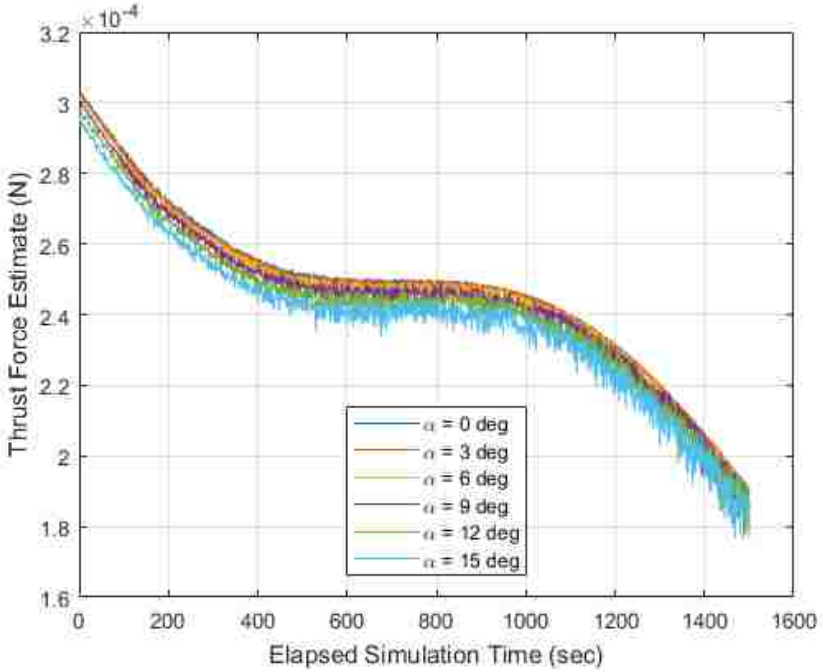

Figure 6.21. Thrust Estimates for Electric Mode using QUEST Centered with Measurement Uncertainty about $\theta = 180°$

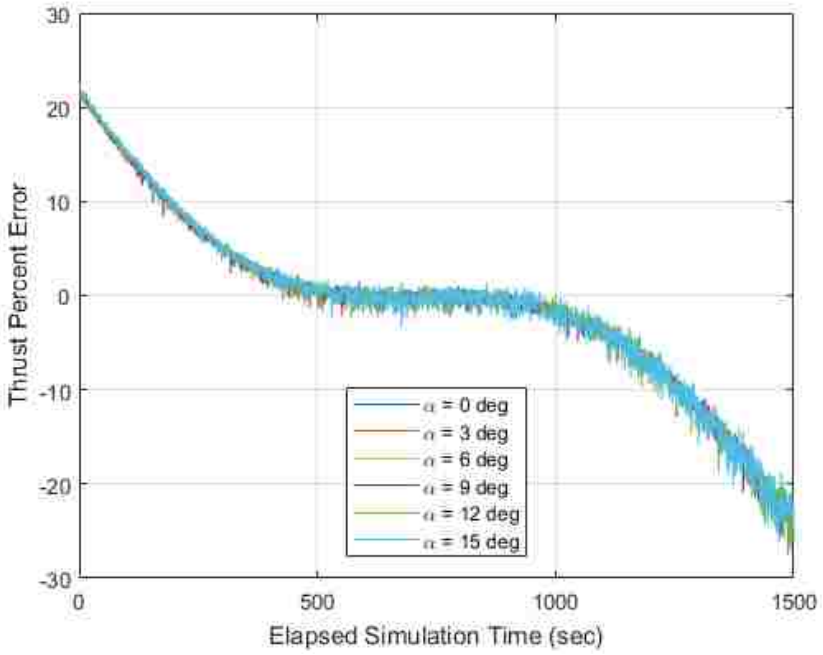

Figure 6.22. Thrust Percent Errors for Electric Mode using QUEST Centered with Measurement Uncertainty about $\theta = 180°$

was within 1% for all cases. The largest effect was from noise being added to the attitude determination system. For the chemical mode the thrust error increased to be within ±3 for all cases. For the electric mode the thrust error varied between 1% to 10% between time-steps depending on the size of the angle α and the location of the maneuver.

6.2. ATTITUDE CHANGING MANEUVER

Based on the results for the orbit changing maneuver, it was decided that an attitude maneuver should be considered as a way of reducing the error in estimating the thrust in the electric mode. To perform an attitude maneuver requires offsetting the thruster from the center of mass to slew the spacecraft. When the thruster is aligned directly with the negative x-axis of the body frame the center of mass and moment of inertia tensor for the prototype spacecraft APEX are

$$\mathbf{X}_{CM} = \begin{bmatrix} 2.184103747 \\ -1.537653632 \\ 16.558218406 \end{bmatrix} \text{ mm} \tag{6.2}$$

$$J = \begin{bmatrix} 91605.676439855 & -149.406238607 & -2429.061164790 \\ -149.406238607 & 119866.404516407 & -205.245669216 \\ -2429.061164790 & -205.245669216 & 47488.115812043 \end{bmatrix} \text{ kg mm}^2 \tag{6.3}$$

The thruster was parametrically offset from the negative x-axis by 1 cm increments along the positive z-axis direction to a maximum of 10 cm. The maximum value was chosen due to physical constraints on the size of APEX. It should be noted that while the location of the thruster was being changed, the center of mass and moment of inertia tensor were kept constant. Ideally the center of mass and moment of inertia matrix would have been updated to reflect the new position of the thruster, however creating a physically realistic structure for each thruster location within APEX was impractical.

Using this method the angular velocity can be directly measured with a gyroscope or an inertial measurement unit (IMU). From the simulation the angular velocities for the array of different offset amounts can be seen in Figures 6.23 and 6.24 for the chemical and electric thrust modes respectively. The thrust estimate and the percent thrust error can be seen in Table 6.1 for chemical mode and Table 6.2 for electric mode. The thrust estimates for both modes are very accurate with errors less than 0.6%.

However, the complication with this maneuver type is that the change in angular velocity is exceptionally large for a CubeSat when performing the chemical mode maneuver. CubeSat-sized reaction wheels are not be able to store the required amount of angular momentum to return the CubeSat to a desired attitude after performing the maneuver. Because one of the goals of this work is to determine a single type of maneuver that can accurately quantify the performance of both modes of the propulsion system, an attitude changing maneuver was not considered a viable option unless an actuator can be integrated that is capable of returning the spacecraft back to zero angular velocity after the maneuver.

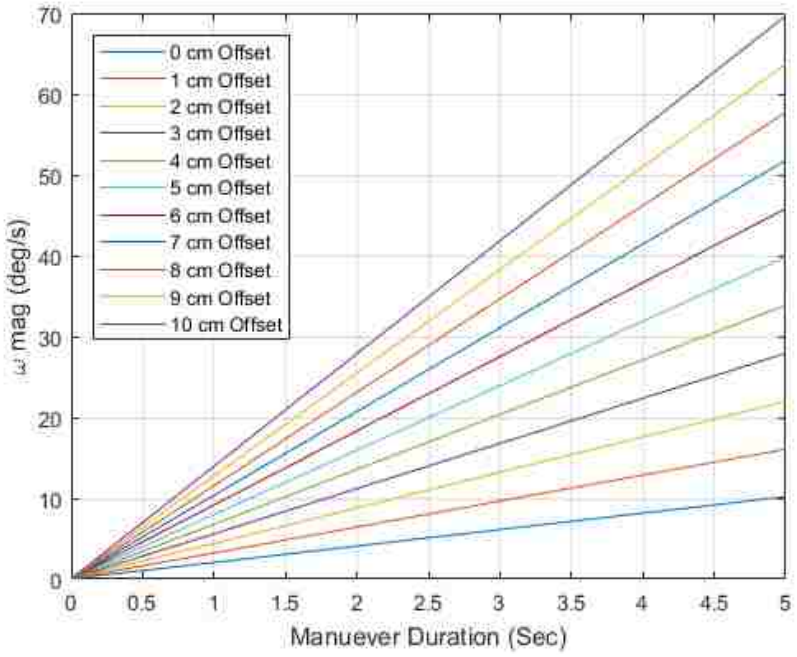

Figure 6.23. Change in Angular Velocity during Chemical Mode Maneuver

Table 6.1. Thrust Estimates and Percent Errors for Chemical Mode Attitude Maneuver

Offset (m)	Thrust Estimate (N)	Percent Error
0	0.248578	-0.568652
0.01	0.249589	-0.164162
0.02	0.249767	-0.093138
0.03	0.249892	-0.043176
0.04	0.249905	-0.037717
0.05	0.249931	-0.027525
0.06	0.249947	-0.020874
0.07	0.249943	-0.022429
0.08	0.249967	-0.013066
0.09	0.249953	-0.018514
0.10	0.249977	-0.009012

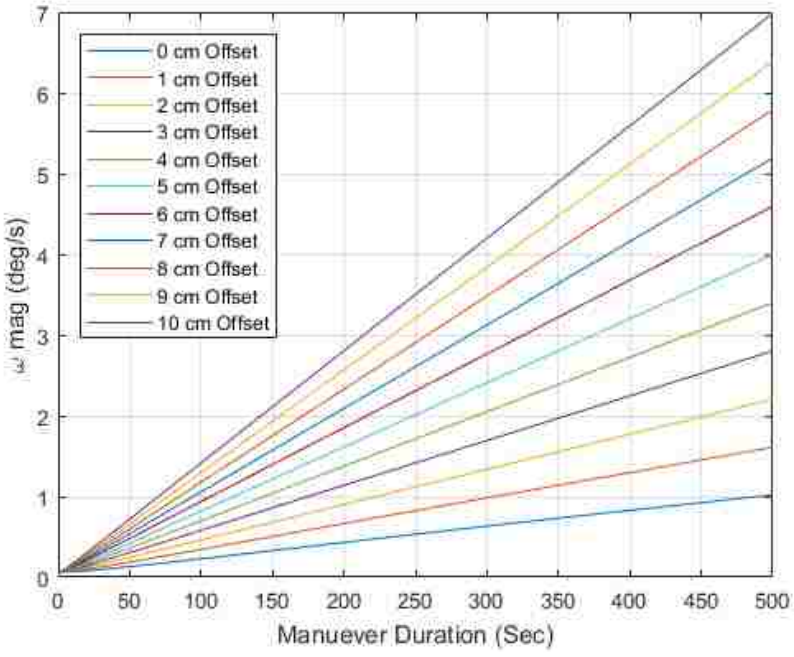

Figure 6.24. Change in Angular Velocity during Electric Mode Maneuver

Table 6.2. Thrust Estimates and Percent Errors for Electric Mode Attitude Maneuver

Offset (m)	Thrust Estimate (mN)	Percent Error
0	0.2495445	-0.1821846
0.01	0.2497803	-0.0878631
0.02	0.2499308	-0.0276766
0.03	0.2499297	-0.0281053
0.04	0.2499704	-0.0118143
0.05	0.2499722	-0.0111088
0.06	0.2499758	-0.0096565
0.07	0.2499867	-0.0052913
0.08	0.2499753	-0.0098424
0.09	0.2499902	-0.0039118
0.10	0.2499769	-0.0092389

7. CONCLUSIONS

7.1. SUMMARY

A study of spacecraft attitude determination and control error effect on quantifying thrust for an experimental micro-propulsion system was performed. An orbit propagator was developed using the Gauss variation of parameters, which included common sources of orbital perturbations when in low Earth orbit. Particular attention was given to the zonal harmonic, J_2, which was included in the derivation for the analytic thrust determination.

Two types of maneuvers were considered to perform thrust determination, a RAAN changing maneuver and an attitude changing maneuver. For the RAAN changing maneuver it was found that varying the direction of the thrust marginally affected being able to accurately perform thrust determination. This is evident in the simulation for the low thrust electric maneuver, where the percent error in the thrust estimate was slightly larger when the thrust direction was oriented away from the $\hat{h}$-direction than when the thrust was entirely in the $\hat{h}$-direction.

A more direct method of performing thrust determination was derived for the attitude changing maneuver. It was found that this method was very accurate in determining the thrust. However, this maneuver also increased the angular velocity beyond a CubeSat's capability of being able to recover its three-axis attitude control for the chemical mode. From these findings this work could not recommend performing an attitude changing maneuver unless the magnitude of the chemical mode thrust is decreased or an alternative method of reducing the angular velocity is implemented.

Two methods for quaternion-based attitude determination, Davenport's q-method and the quaternion estimator (QUEST) were discussed. This work chose to implement QUEST because it is the most common approach to performing attitude determination.

With no measurement uncertainty using the results from the QUEST algorithm were nearly identical to the results when the true attitude state was used. When measurement uncertainty was added to the sensors the error in thrust determination increased moderately. As the pointing for the thrust angled away from the desired $\hat{h}$-direction the amount of error in the thrust determination increased as well.

7.2. FUTURE WORK

When deriving the equations for the analytic thrust determination a few assumptions were made, i.e. that the orbit is circular ($e = 0$), the thrust is constant in direction and magnitude, and the change in inclination is negligible. However, to perform the propagation of the orbit trajectory it was necessary to use a small eccentricity because the Gauss VOP equations are undefined for circular orbits. This meant that the radius r and the angular momentum h would not be constant during the maneuver, especially for the electric mode where the maneuver lasts for approximately one fourth of a revolution of the orbit. By relaxing this assumption it could improve the accuracy of the thrust determination estimates that were over-estimating the thrust for the electric mode.

The other assumption that should be relaxed is that the change in inclination is negligible. This assumption was made because the location of the maneuver was originally chosen to be about $\theta = 90°$, where the change in inclination was minimized. However, centering about this location led to large errors in estimating the thrust, so the maneuver was moved to be about $\theta = 180°$. At this new location the change in inclination would now be maximized, and the assumption that the change in inclination is negligible may no longer be valid. By removing this assumption the accuracy of the thrust estimate could change when performed about the location $\theta = 180°$. It is also of significant interest to determine the reason why thrust errors are increased when the maneuver is executed near $\theta = 90°$. This determination could have a significant impact on how APEX's Concept of Operations are finalized.

In addition to the previous suggestions, more work can be done to relax the assumption that the reaction wheels cannot saturate. To do this another type of actuator should be included to desaturate the reaction wheels as necessary and a new control law would need to be defined that includes both actuators. This would also be beneficial because as was shown in Section 6.1.1.2 the current control law is unable to produce enough torque to hold the correct pointing during the electric mode maneuver. More work could be done by considering attitude errors about all of the LVLH frame axes, as opposed to just the $\hat{r}$-direction considered in this study. This could be done by creating a Monte Carlo simulation to compare the effects of attitude error about any single axis and combinations of all the axes. The QUEST algorithm's attitude estimate can be improved by incorporating different types of attitude sensors and by appropriately weighting the sensor measurements. Another method of improving QUEST's attitude estimate would be to add a sensor measurement filter to reduce the effect of the measurement uncertainty. Higher-fidelity models could be implemented to increase the precision in the perturbing forces, as well as creating a more complex model for the external surfaces that the perturbing forces are acting upon.

APPENDIX A.

WORLD MAGNETIC MODEL 2015

The World Magnetic Model (WMM) 2015 is an approximation for modeling the Earth's magnetic field and is possible through the collaboration of many different researchers [28]. The procedure shown here to implement the magnetic model follows from their report. In order to implement the magnetic model requires using specific model coefficients that can be found at the National Oceanic and Atmospheric Administration (NOAA) website [29]. NOAA also provides software in both C and Fortran to calculate the magnetic field.

The magnetic field $\mathbf{B}_m$ is described by seven elements: the three field vector components (X the northerly intensity, Y the easterly intensity, and Z the vertical intensity (positive downwards)) and four more quantities derived from the vector components (H the horizontal intensity, F the total intensity, I the inclination angle, and D the declination angle). All of the variables adhere to the following unit conventions: the field vector components and the intensities are in nano-Teslas (nT), angles are in radians, lengths are in meters, and times are in years.

The magnetic field is a potential field which can be written in geocentric spherical coordinates (longitude λ, latitude φ', and radius r) as the negative gradient of a scalar potential

$$\mathbf{B}_m(\lambda, \varphi', r, t) = -\nabla V(\lambda, \varphi', r, t) \tag{1}$$

The potential can be expanded in terms of spherical harmonics as

$$V(\lambda, \varphi', r, t) = a \sum_{n=1}^{N} \left(\frac{a}{r}\right)^{n+1} \sum_{m=0}^{n} (g_n^m(t) \cos(m\lambda) + h_n^m(t) \sin(m\lambda)) \breve{\mathrm{P}}_n^m(\sin \varphi') \tag{2}$$

where $N = 12$ is the degree of the expansion of the WMM, a (6,371,200 m) is the geomagnetic reference radius, and $g_n^m(t)$ and $h_n^m(t)$ are the time-dependent Gauss coefficients of degree n and order m describing the Earth's main magnetic field. For any real number μ

and $\breve{\mathrm{P}}_n^m(\mu)$ are the Schmidt semi-normalized associated Legendre functions

$$\begin{aligned} \breve{\mathrm{P}}_n^m(\mu) &= \sqrt{2\frac{(n-m)!}{(n+m)!}} P_{n,m}(\mu) \quad \text{if} \quad m > 0 \\ \breve{\mathrm{P}}_n^m(\mu) &= P_{n,m}(\mu) \quad \text{if} \quad m = 0 \end{aligned} \tag{3}$$

where $P_{n,m}$ are the same associated Legendre functions used to calculate the zonal harmonics in Section 2.3.1.

To determine the magnetic field at a specific time and location, the first step is to transform the geodetic coordinates (longitude λ, geodetic latitude φ, and height h above the WGS 84 ellipsoid) into spherical geocentric coordinates. The WGS 84 ellipsoid is defined by the semimajor axis A, the reciprocal flattening $1/f$, the eccentricity squared e^2, and the radius of curvature of the prime vertical R_c at a given latitude as

$$A = 6,378,137 \text{ m} \tag{4}$$

$$\frac{1}{f} = 298.257223563 \tag{5}$$

$$e^2 = f(2-f) \tag{6}$$

$$R_c = \frac{A}{\sqrt{1 - e^2 \sin^2 \varphi}} \tag{7}$$

In the transformation from geodetic to spherical geocentric the longitude λ is the same in both coordinate systems and the latitude and the radius can be found from

$$p = (R_c + h) \cos \varphi \tag{8}$$

$$z = (R_c(1 - e^2) + h) \sin \varphi \tag{9}$$

$$r = \sqrt{p^2 + z^2} \tag{10}$$

$$\varphi' = \arcsin \frac{z}{r} \tag{11}$$

The second step is to determine the Gauss coefficients $g_n^m(t)$ and $h_n^m(t)$ for a desired time as

$$\begin{aligned} g_n^m(t) &= g_n^m(t_0) + (t - t_0)\dot{g}_n^m(t_0) \\ h_n^m(t) &= h_n^m(t_0) + (t - t_0)\dot{h}_n^m(t_0) \end{aligned} \tag{12}$$

where the time t is given in decimal years, $t_0 = 2015.0$, $g_n^m(t_0)$ and $h_n^m(t_0)$ are the main field coefficients, and $\dot{g}_n^m(t_0)$ and $\dot{h}_n^m(t_0)$ are the secular variation coefficients.

The third step is to find the field vector components X', Y', and Z' in geocentric coordinates that are computed as

$$\begin{aligned} X'(\lambda, \varphi', r) &= -\frac{1}{r}\frac{\partial V}{\partial \varphi'} \\ &= -\sum_{n=1}^{12}\left(\frac{a}{r}\right)^{n+2}\sum_{m=0}^{n}(g_n^m(t)\cos m\lambda + h_n^m(t)\sin m\lambda)\frac{d\breve{\mathrm{P}}_n^m(\sin\varphi')}{d\varphi'} \end{aligned} \tag{13}$$

$$\begin{aligned} Y'(\lambda, \varphi', r) &= -\frac{1}{r\cos\varphi'}\frac{\partial V}{\partial \lambda} \\ &= \frac{1}{\cos\varphi'}\sum_{n=1}^{12}\left(\frac{a}{r}\right)^{n+2}\sum_{m=0}^{n} m(g_n^m(t)\sin m\lambda - h_n^m(t)\cos m\lambda)\breve{\mathrm{P}}_n^m(\sin\varphi') \end{aligned} \tag{14}$$

$$\begin{aligned} Z'(\lambda, \varphi', r) &= \frac{\partial V}{\partial r} \\ &= -\sum_{n=1}^{12}(n+1)\left(\frac{a}{r}\right)^{n+2}\sum_{m=0}^{n}(g_n^m(t)\cos m\lambda + h_n^m(t)\sin m\lambda)\breve{\mathrm{P}}_n^m(\sin\varphi') \end{aligned} \tag{15}$$

The secular variation of the field vector components can be found using

$$\begin{aligned} \dot{X}'(\lambda, \varphi', r) &= -\frac{1}{r}\frac{\partial \dot{V}}{\partial \varphi'} \\ &= -\sum_{n=1}^{12}\left(\frac{a}{r}\right)^{n+2}\sum_{m=0}^{n}(\dot{g}_n^m\cos m\lambda + \dot{h}_n^m\sin m\lambda)\frac{d\breve{\mathrm{P}}_n^m(\sin\varphi')}{d\varphi'} \end{aligned} \tag{16}$$

$$\begin{aligned} \dot{Y}'(\lambda, \varphi', r) &= -\frac{1}{r\cos\varphi'}\frac{\partial \dot{V}}{\partial \lambda} \\ &= \frac{1}{\cos\varphi'}\sum_{n=1}^{12}\left(\frac{a}{r}\right)^{n+2}\sum_{m=0}^{n} m(\dot{g}_n^m\sin m\lambda - \dot{h}_n^m\cos m\lambda)\breve{\mathrm{P}}_n^m(\sin\varphi') \end{aligned} \tag{17}$$

$$\begin{aligned}\dot{Z}'(\lambda,\varphi',r) =& \frac{\partial \dot{V}}{\partial r} \\ =& -\sum_{n=1}^{12}(n+1)\left(\frac{a}{r}\right)^{n+2}\sum_{m=0}^{n}(\dot{g}_n^m \cos m\lambda + \dot{h}_n^m \sin m\lambda)\breve{\mathrm{P}}_n^m(\sin\varphi')\end{aligned} \tag{18}$$

where

$$\frac{d\breve{\mathrm{P}}_n^m(\sin\varphi')}{d\varphi'} = (n+1)(\tan\varphi')\,\breve{\mathrm{P}}_n^m(\sin\varphi') - \sqrt{(n+1)^2 - m^2}\,(\sec\varphi')\,\breve{\mathrm{P}}_{n+1}^m(\sin\varphi') \tag{19}$$

The field vector components can be rotated into the ellipsoidal reference frame using

$$\begin{aligned} X &= X'\cos(\varphi'-\varphi) - Z'\sin(\varphi'-\varphi) \\ Y &= Y' \\ Z &= X'\sin(\varphi'-\varphi) + Z'\cos(\varphi'-\varphi) \end{aligned} \tag{20}$$

Similarly, the secular variations of the vector components are rotated using

$$\begin{aligned} \dot{X} &= \dot{X}'\cos(\varphi'-\varphi) - \dot{Z}'\sin(\varphi'-\varphi) \\ \dot{Y} &= \dot{Y}' \\ \dot{Z} &= \dot{X}'\sin(\varphi'-\varphi) + \dot{Z}'\cos(\varphi'-\varphi) \end{aligned} \tag{21}$$

Lastly, the remaining magnetic elements H, F, I, and D are calculated from the orthogonal components using

$$\begin{aligned} H &= \sqrt{X^2+Y^2} \\ F &= \sqrt{X^2+Y^2+Z^2} \\ I &= \tan^{-1}\left(\frac{Z}{H}\right) \\ D &= \tan^{-1}\left(\frac{Y}{X}\right) \end{aligned} \tag{22}$$

where performing a quadrant check and avoiding division by zero results in a range for the declination of $-\pi$ to π and a range for the inclination of $-\pi/2$ to $\pi/2$. The secular variations of these elements $\dot{H}$, $\dot{F}$, $\dot{I}$, and $\dot{D}$ are calculated using

$$\begin{aligned} \dot{H} &= \frac{X\dot{X} + Y\dot{Y}}{H} \\ \dot{F} &= \frac{X\dot{X} + Y\dot{Y} + Z\dot{Z}}{F} \\ \dot{I} &= \frac{H\dot{Z} - Z\dot{H}}{F^2} \\ \dot{D} &= \frac{X\dot{Y} - Y\dot{X}}{H^2} \end{aligned} \tag{23}$$

where $\dot{I}$ and $\dot{D}$ are given in radians per year.

APPENDIX B.

MATLAB MODEL VERIFICATION

To verify the accuracy of the models implemented in this study, analogous scenarios were created in the program Systems Tool Kit (STK) developed by Analytic Graphics, Inc. The same initial state was used in all of the STK scenarios and was chosen based on the Keplerian elements at the time of the start of the maneuvers in the MATLAB models. This was to ensure that both STK and the MATLAB models were using the same initial conditions, which are shown in Figure 1. Along with the initial conditions all of the STK scenarios used the Astrogator propagator with the "Earth J2" propagator model chosen for the central body that the satellite would orbit. This model assumes a two-body propagation and includes the perturbing effects of the zonal harmonic J_2. A few of the constants from the "Earth J2" model are shown in Table 1.

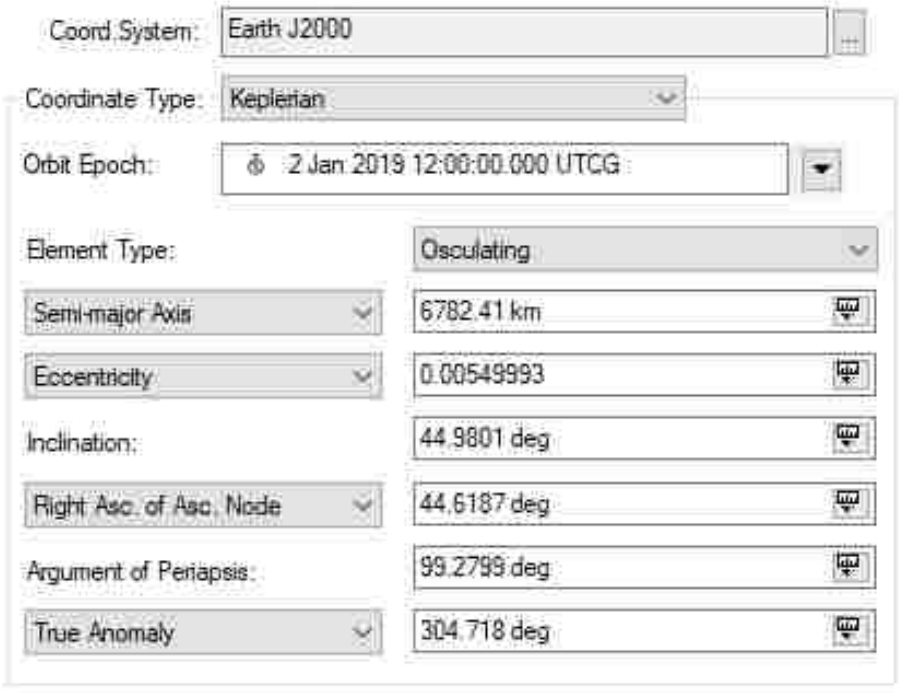

Figure 1. Initial Conditions for STK Scenario

Table 1. STK Parameters for Earth

Radius	Gravitational Parameter	Zonal Harmonic, J_2
6378.14 km	398600 km^3/sec^2	0.00108263

The first STK scenario created to verify the MATLAB models was purely a time propagation without a maneuver to verify adding the J_2 perturbation to the Gauss variation of parameters. To do this the simulations were propagated for 10 hours and in STK the Earth J_2 setting was chosen for the central body to only include the perturbations from the zonal harmonic J_2. Figures 2-8 show the propagation of the Keplerian elements for both the STK scenario and the MATLAB model on the left and the difference between the STK and MATLAB values is shown on the right. From the difference plots it can be seen that there is a small discrepancy between the propagation of the Keplerian elements from the two programs, however this is believed to be from rounding errors when converting the STK propagation from Cartesian to Keplerian for plotting purposes. The spikes that occur in the difference plot for Figure 7 are because the true anomaly crossed from 360° to 0° at different intervals in STK and MATLAB.

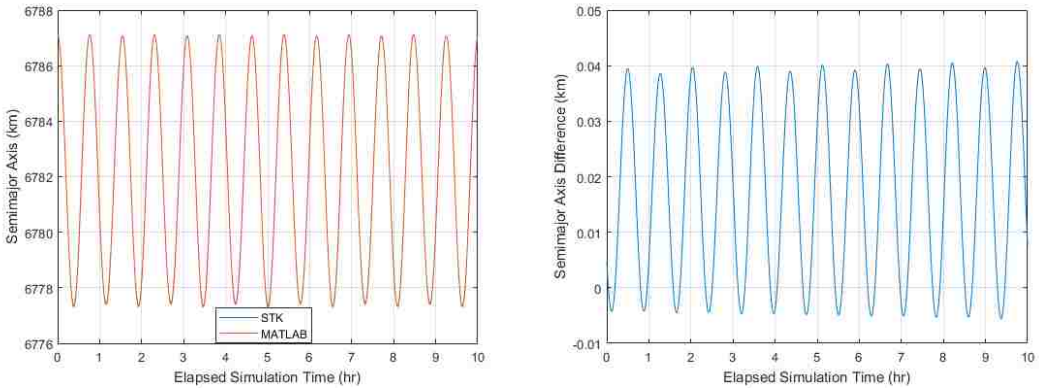

(a) Comparison (b) Difference

Figure 2. Propagation Comparison and Difference for Semimajor Axis

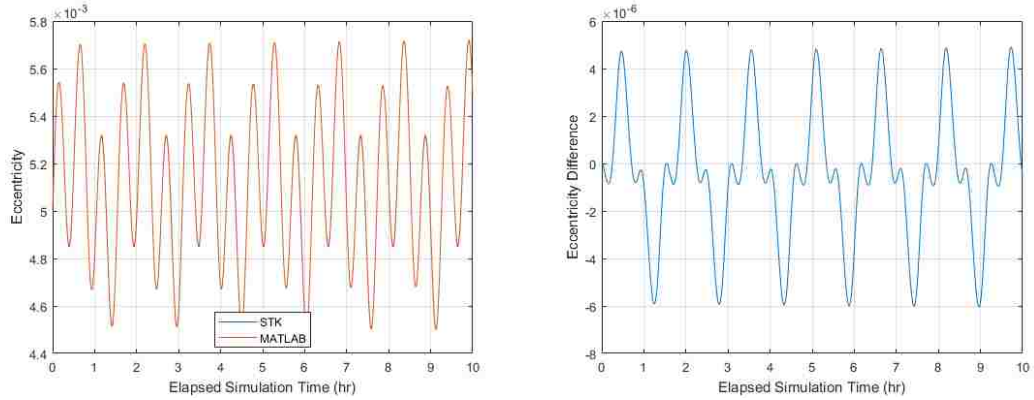

(a) Comparison (b) Difference

Figure 3. Propagation Comparison and Difference for Eccentricity

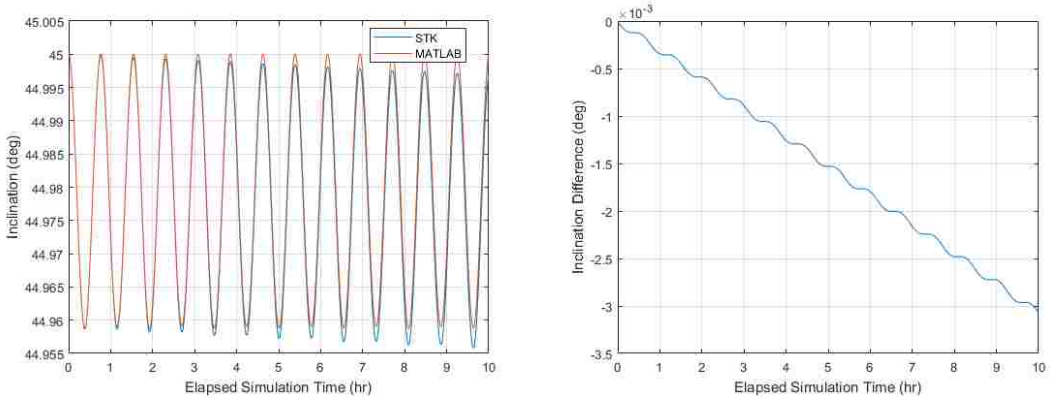

(a) Comparison (b) Difference

Figure 4. Propagation Comparison and Difference for Inclination

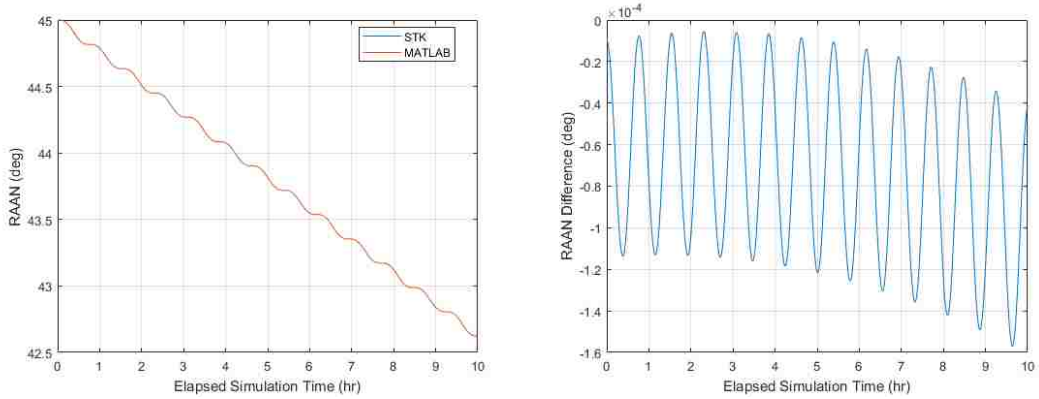

(a) Comparison (b) Difference

Figure 5. Propagation Comparison and Difference for Right Ascension of Ascending Node

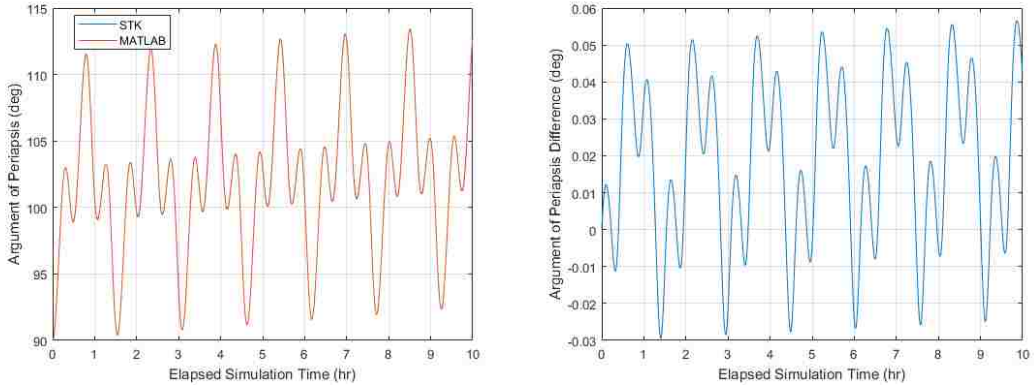

(a) Comparison (b) Difference

Figure 6. Propagation Comparison and Difference for Argument of Periapsis

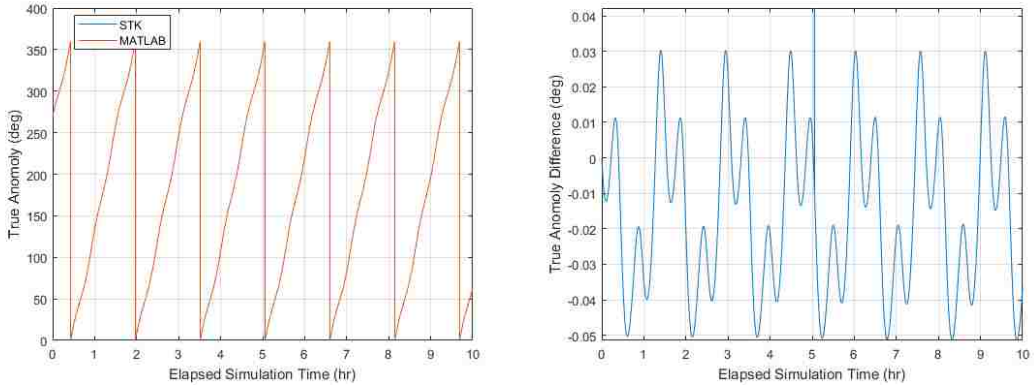

(a) Comparison (b) Difference

Figure 7. Propagation Comparison and Difference for True Anomaly

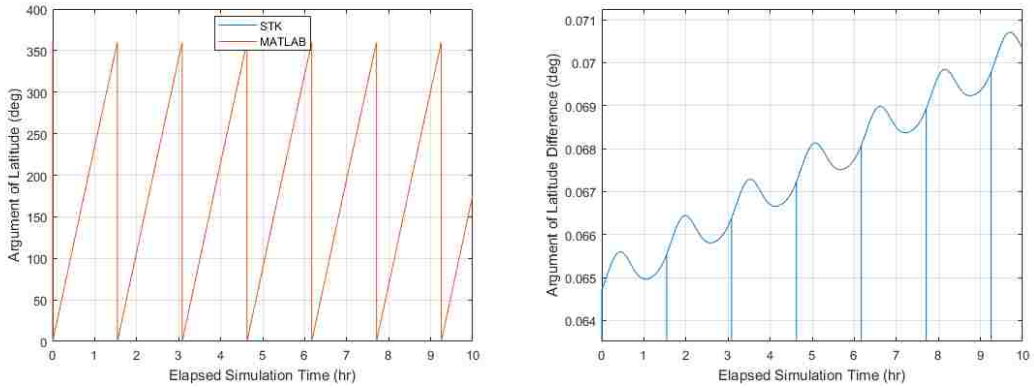

(a) Comparison (b) Difference

Figure 8. Propagation Comparison and Difference for Argument of Latitude

The second STK scenario created was to simulate the change in the orbital elements when performing an electric mode (0.25 mN thrust) maneuver centered about an argument of latitude of 90°, with the thrust pointing in the $\hat{h}$-direction of the LVLH frame for the entire maneuver. The results for this maneuver are shown in Figures 9-15. Similar to the no maneuver case, there are small differences in the Keplerian elements between the STK scenario and the MATLAB models. The largest differences are in the argument of periapsis and the true anomaly, where the differences nearly reach a value of 0.05°. These larger differences seen when performing a maneuver are believed to be because STK considers the change in mass from burning propellant, whereas the MATLAB models consider the mass to be constant for the entire simulation. Overall, the differences in the Keplerian elements between the STK scenario and the MATLAB models are very small for an electric mode maneuver.

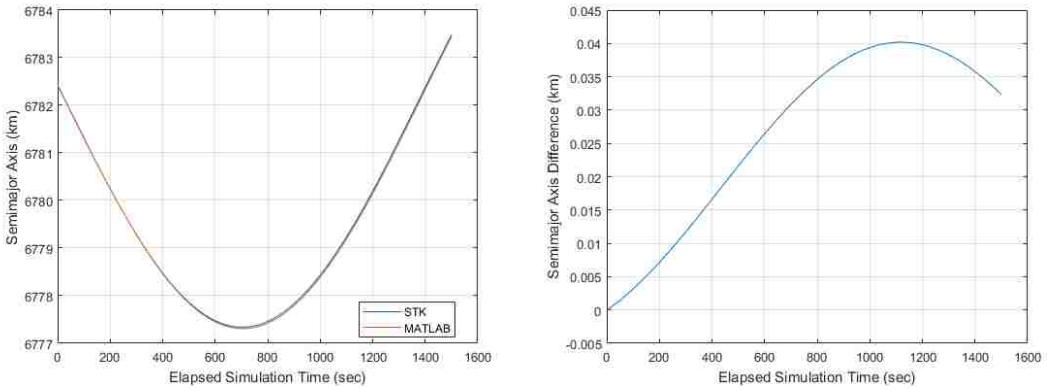

(a) Comparison (b) Difference

Figure 9. Electric Mode Maneuver Comparison and Difference for Semimajor Axis

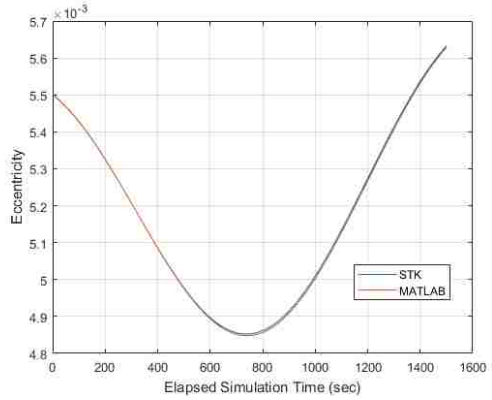

(a) Comparison

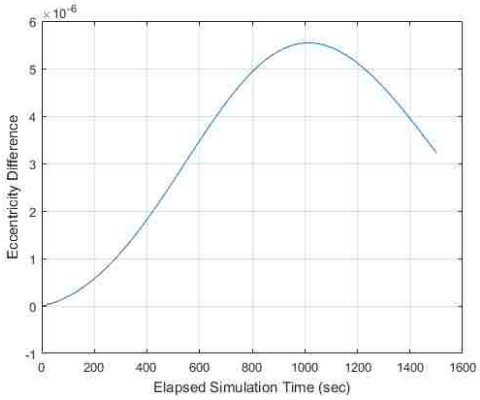

(b) Difference

Figure 10. Electric Mode Maneuver Comparison and Difference for Eccentricity

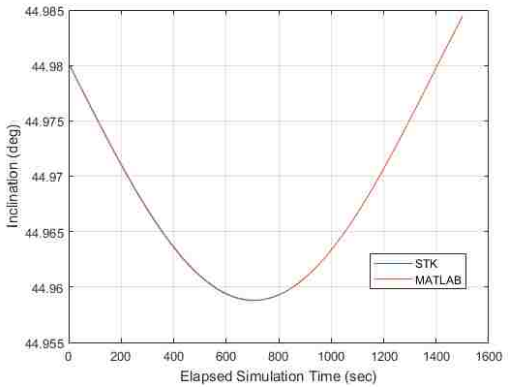

(a) Comparison

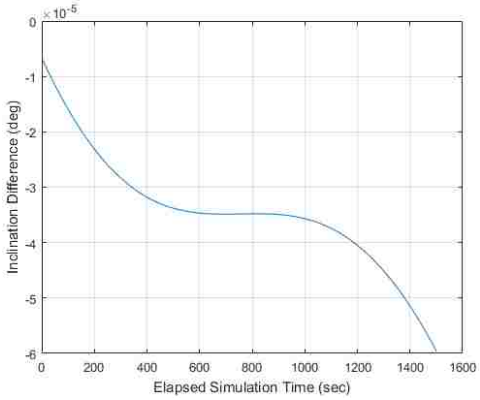

(b) Difference

Figure 11. Electric Mode Maneuver Comparison and Difference for Inclination

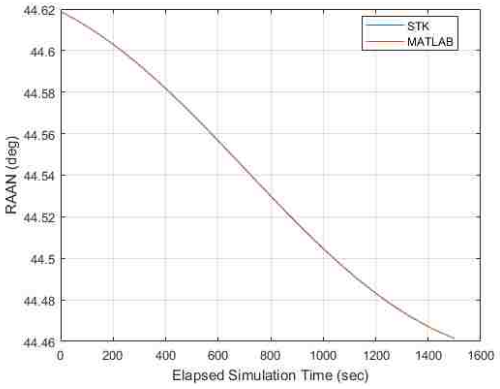

(a) Comparison

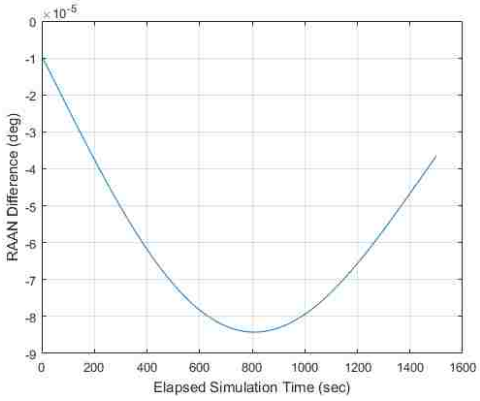

(b) Difference

Figure 12. Electric Mode Maneuver Comparison and Difference for Right Ascension of Ascending Node

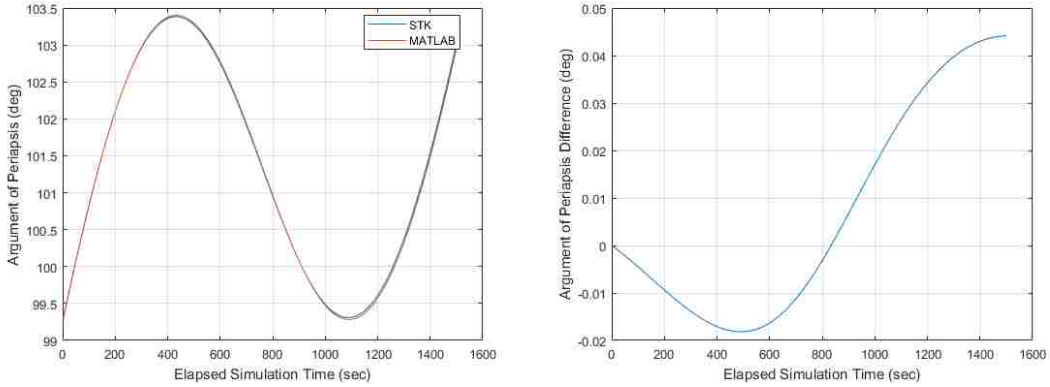

(a) Comparison (b) Difference

Figure 13. Electric Mode Maneuver Comparison and Difference for Argument of Periapsis

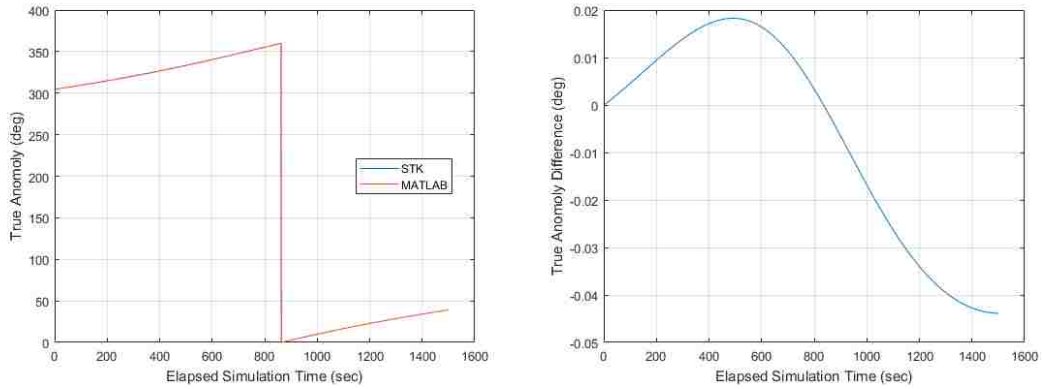

(a) Comparison (b) Difference

Figure 14. Electric Mode Maneuver Comparison and Difference for True Anomaly

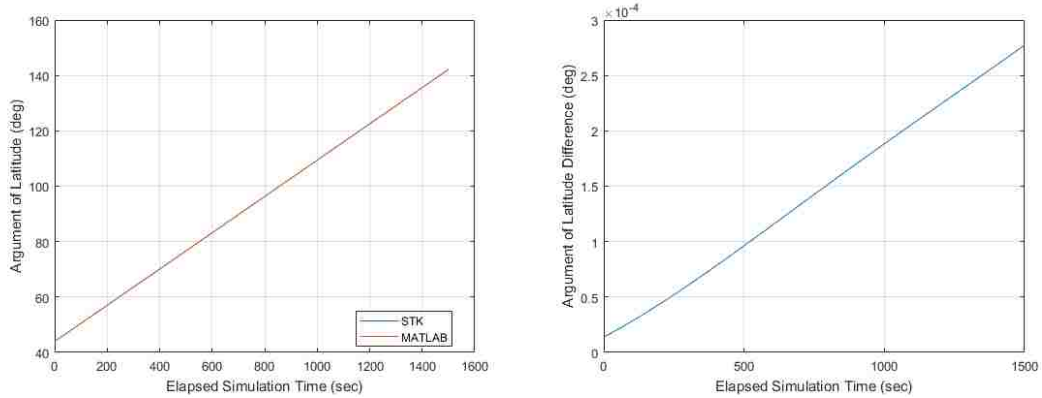

(a) Comparison (b) Difference

Figure 15. Electric Mode Maneuver Comparison and Difference for Argument of Latitude

A final STK scenario was created to test an extreme case where the satellite would hypothetically produce 10 Newtons of thrust. This thrust force is realistically impossible for the satellite APEX to produce, however this thrust was included as a method of analyzing the MATLAB models to an extreme degree. Except for the change in the thrust value, all of the initial conditions and the maneuver were held the same as the previous comparison. The results from this maneuver are shown in Figures 16-22. For this maneuver all of the Keplerian elements are fairly different by the end of the maneuver. This is again believed to be because STK considers the change in mass for the satellite as the maneuver continues. To produce the large thrust would require having a larger mass flow rate ($\dot{m} = 0.000255$ kg/s), meaning the total change in mass would be 0.382 kg for the entire maneuver. Clearly, this change in mass is too large to be considered negligible. Because the MATLAB model maintains constant mass for the duration of the maneuver this is believed to be the reason for the large differences. To confirm the change in mass as the cause for the differences, the STK scenario was performed a second time with a larger mass flow rate ($\dot{m} = 0.0102$ kg/s). When comparing this run of the scenario to the MATLAB results the differences in all of the Keplerian elements were significantly larger. For example by the end of the maneuver the difference in RAAN was $-8.394°$ for the larger mass flow rate, whereas for the smaller mass flow rate the difference was $-1.136°$. By performing this scenario with the two different mass flow rates the differences between STK and MATLAB were confirmed to be due to the change in mass.

Based on these results, it is believed that the MATLAB simulation accurately models APEX's orbital motion. Attitude model verification still needs to be performed as of this time.

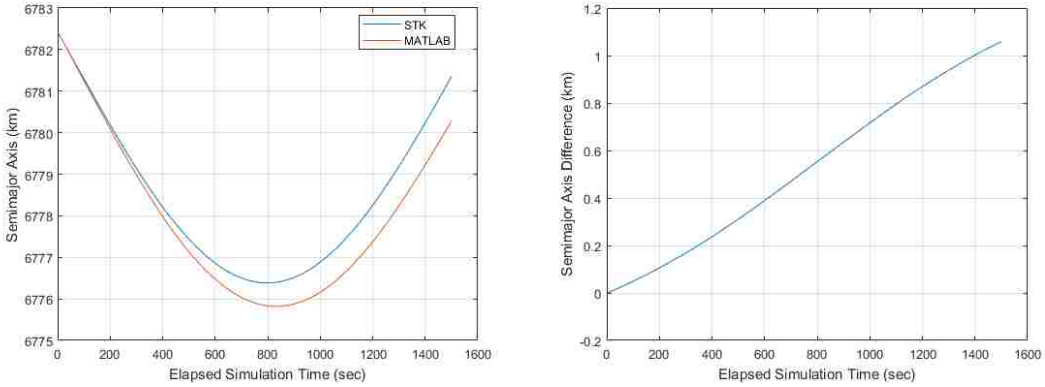

(a) Comparison (b) Difference

Figure 16. 10 N Thrust Maneuver Comparison and Difference for Semimajor Axis

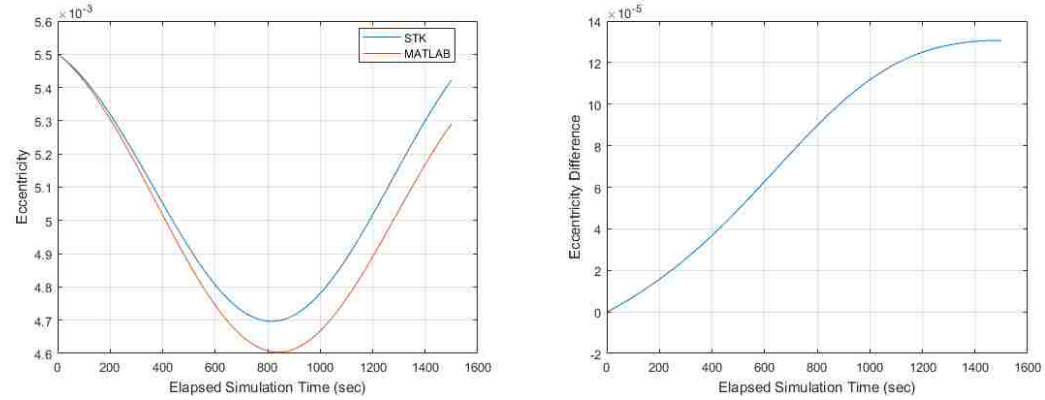

(a) Comparison (b) Difference

Figure 17. 10 N Thrust Maneuver Comparison and Difference for Eccentricity

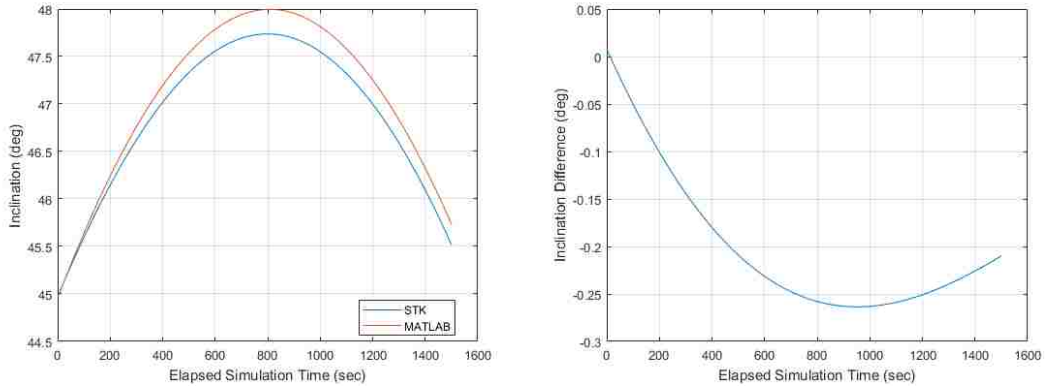

(a) Comparison (b) Difference

Figure 18. 10 N Thrust Maneuver Comparison and Difference for Inclination

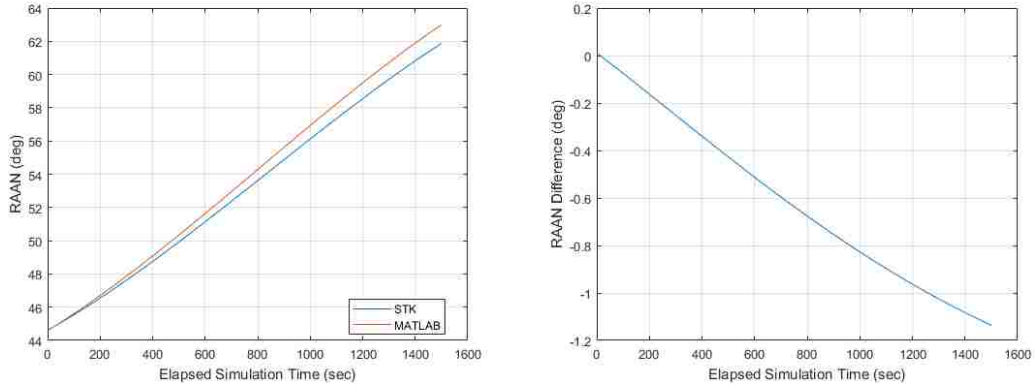

(a) Comparison (b) Difference

Figure 19. 10 N Thrust Maneuver Comparison and Difference for Right Ascension of Ascending Node

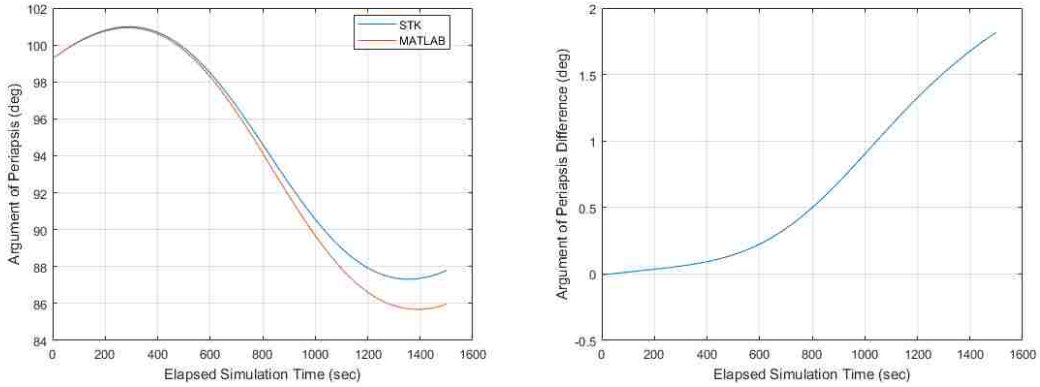

(a) Comparison (b) Difference

Figure 20. 10 N Thrust Maneuver Comparison and Difference for Argument of Periapsis

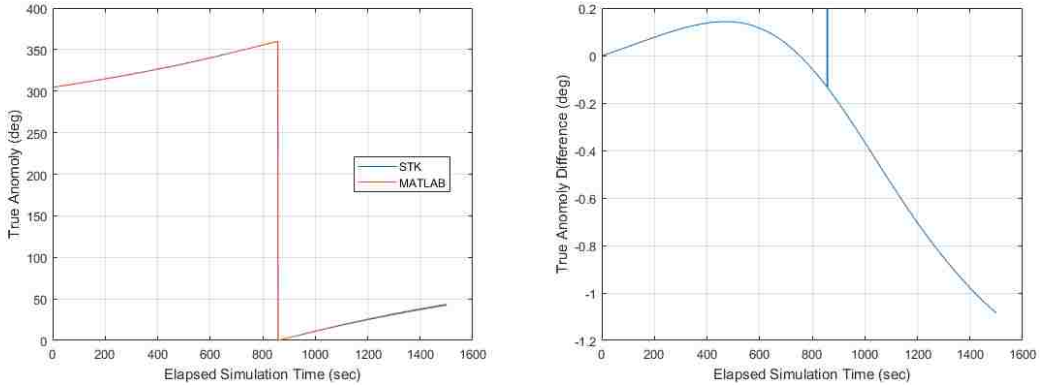

(a) Comparison (b) Difference

Figure 21. 10 N Thrust Maneuver Comparison and Difference for True Anomaly

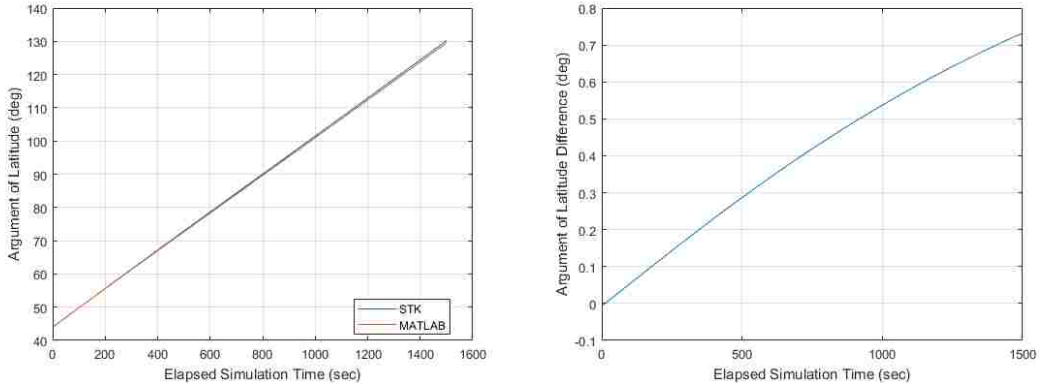

(a) Comparison (b) Difference

Figure 22. 10 N Thrust Maneuver Comparison and Difference for Argument of Latitude

REFERENCES

[1] C.C. Liebe. "Accuracy Performance of Star Trackers - A Tutorial." *IEEE Transactions on Aerospace and Electronic Systems*, 2002. ISSN 00189251. doi: 10.1109/TAES.2002.1008988.

[2] Landis Markley. "Attitude Determination from Vector Observations: A Fast Optimal Matrix Algorithm." *The Journal of the Astronautical Sciences*, 41(2):261–280, 1993.

[3] Steven P. Berg and Joshua L. Rovey. "Assessment of Multimode Spacecraft Micropropulsion Systems." *Journal of Spacecraft and Rockets*, 54:592–601, 2017.

[4] Kathleen Zona. "Ion Propulsion: Farther, Faster, Cheaper." *NASA Glenn Research Center*, 2004.

[5] Andrew J Jamison, Andrew D Ketsdever, and E P Muntz. "Accurate Measurement of Nano-Newton Thrust for Micropropulsion System Characterization." In *27th International Electric Propulsion Conference*, 2001.

[6] Johan Köhler, Johan Bejhed, Henrik Kratz, Fredrik Bruhn, Ulf Lindberg, Klas Hjort, and Lars Stenmark. "A Hybrid Cold Gas Microthruster System for Spacecraft." *Sensors and Actuators, A: Physical*, 97(98):587–598, 2002.

[7] C. Rossi, T. Do Conto, D. Estève, and B. Larangot. "Design, Fabrication and Modeling of MEMS-Based Microthrusters for Space Application." *Smart Materials and Structure*, 10:1156–1162, 2001.

[8] M. Gamero-Castano and V. Hruby. "Electrospray as a Source of Nanoparticles for Efficient Colloid Thrusters." In *36th AIAA/ASME/SAE/ASEE Joint Propulsion Conference and Exhibit*. American Institute of Aeronautics and Astronautics, 2000.

[9] *Space Vehicle Accelerometer Applications*. National Aeronautics and Space Administration (NASA), 1972. URL `https://books.google.com/books?id=m8pQAAAAYAAJ`.

[10] Tom Kelecy and Moriba Jah. "Detection and Orbit determination of a Satellite Executing Low Thrust Maneuvers." *Acta Astronautica*, 66:798–809, 2010.

[11] W. R. Kerslake, R. G. Goldman, and W. C. Nieberding. "SERT II - Mission, Thruster Performance, and In-Flight Thrust Measurements." *Journal of Spacecraft and Rockets*, 8(3):213–224, 1971.

[12] G. Manzoni and Yesie L. Brama. "Cubesat Micropropulsion Characterization in Low Earth Orbit." In *Proceedings of the AIAA/USU Confernece on Small Satellites*, number SS15-IV-5, 2015. URL `https://digitalcommons.usu.edu/smallsat/2015/all2015/26/`.

[13] A. Macario-Rojas and K. L. Smith. "Spiral Coning Manoeuvre for In-Orbit Low Thrust Characterisation in CubeSats." *Aerospace Science and Technology*, 71:337–346, 2017.

[14] Bradyn Morton and Shannah Withrow-Maser. "On-Orbit CubeSat Performance Validation of a Multi-Mode Micropropulsion System." *Proceedings of the AIAA/USU Conference on Small Satellites, Frank J. Redd Student Scholarship Competition*, (SS17-VIII-4), 2017.

[15] Steven P. Berg. *"Development of Ionic Liquid Multi-Mode Spacecraft Micropropulsion Systems."* PhD thesis, Missouri University of Science and Technology, 2015.

[16] R.H. Battin. *An Introduction to the Mathematics and Methods of Astrodynamics, Revised Edition*. AIAA Education Series. American Institute of Aeronautics and Astronautics, Inc., 1999. ISBN 9781563473425.

[17] D.A. Vallado and W.D. McClain. *Fundamentals of Astrodynamics and Applications*. Space Technology Library. Microcosm Press, 2013. ISBN 9781881883180.

[18] F.Landis Markley and John.L Crassidis. *Fundamentals of Spacecraft Attitude Determination and Control*. Space Technology Library. Microcosm Press and Springer, 2014. ISBN 9781493908011.

[19] C. Fröhlich and J. Lean. "Total Solar Irradiance (TSI) Composite Database (1978-present)", (Accessed March 26, 2019). URL `http://www.ngdc.noaa.gov/stp/solar/solarirrad.html#composite`.

[20] B.W. Morton. "Quantifying On-Orbit Performance of Cubesat Micropropulsion Systems by Observing Orbital Element Variations." Master's thesis, Missouri University of Science and Technology, 2018.

[21] Harold D. Black. "A Passive System for Determining the Attitude of a Satellite." *AIAA Journal*, 2(7):1350–1351, 1964.

[22] Grace Wahba. "A Least-Squares Estimate of Satellite Attitude." *SIAM Review*, 7(3): 409, July, 1965.

[23] James R. Wertz, editor. *Spacecraft Attitude Determination and Control*. D. Reidel Publishing Company, 1985.

[24] Francis B. Hildebrand. *Advanced Calculus for Applications*. Englewood Cliffs, NJ, Prentice-Hall, Inc., 1962.

[25] M.D. Shuster and S.D. Oh. "Attitude Determination from Vector Observations." *Journal of Guidance and Control*, 4(1):70–77, 1981.

[26] W.G. Kelley and A.C. Peterson. *The Theory of Differential Equations Classical and Qualitative*. Springer, 2010.

[27] NanoRacks CubeSat Deployer (NRCSD) Interface Definition Document (IDD). Technical report, 2018.

[28] A. Chulliat, S. Macmillan, P. Alken, C. Beggan, M. Nair, B. Hamilton, A. Woods, V. Ridley, S. Maus, and A. Thomson. "The US/UK World Magnetic Model for 2015-2020 Technical Report." Technical report, NOAA National Geophysical Data Center, Boulder, CO, 2015. doi: 10.7289/V5TB14V7.

[29] World Magnetic Model - Software Download, (Accessed March 25, 2019). URL https://www.ngdc.noaa.gov/geomag/WMM/soft.shtml.

VITA

Andrew Watson was born in 1994, in St. Peters, Missouri. In August 2013 he began his collegiate career at the Missouri University of Science and Technology. He graduated Cum Laude with a Bachelors of Science degree in Aerospace Engineering in May 2017. Andrew started graduate school in August 2017 at the Missouri University of Science and Technology in pursuit of a Masters degree in Aerospace Engineering in the area of Guidance, Navigation, and Control. In July 2019 he received his Masters of Science degree in Aerospace Engineering from the Missouri University of Science and Technology.